

Non-Hermitian physics in the many-body system of Rydberg atoms

Ya-Jun Wang^{1,2,†}, Jun Zhang^{1,2,†}, and Dong-Sheng Ding^{1,2,*}

¹*Key Laboratory of Quantum Information, University of Science and Technology of China, Hefei, Anhui 230026, China. and*

²*Synergetic Innovation Center of Quantum Information and Quantum Physics,
University of Science and Technology of China, Hefei, Anhui 230026, China.*

(Dated: February 10, 2026)

I. ABSTRACT

Non-Hermitian physics exhibits unique physical properties beyond those of traditional Hermitian systems, such as symmetry breaking, the emergence of exceptional points, topological phase transitions, and more. These phenomena have been extensively studied across various platforms, including quantum optics, cold atom systems, superconducting circuits, and condensed matter physics. Rydberg atoms, with their long-range interactions and flexible controllability, provide a promising platform for the experimental realization of non-Hermitian physics. This review primarily summarizes the key experimental and theoretical achievements in the field of non-Hermitian physics within Rydberg atomic systems in recent years. It outlines the fundamental construction of non-Hermitian Hamiltonians, reveals the effective dissipation mechanisms induced by Rydberg atomic interactions, and discusses their impact on spectral properties and symmetry breaking. These studies not only deepen the understanding of quantum phase transitions in non-Hermitian many-body systems but also highlight the unique value of Rydberg atomic platforms in realizing and controlling topological states.

II. INTRODUCTION

In conventional quantum mechanics, Hamiltonians are typically Hermitian, ensuring real-valued energy eigenvalues. However, non-Hermitian Hamiltonians allow for complex eigenvalues [1–4], corresponding to non-conservative dynamics with gain or dissipation, and exhibit unique physical behaviors across a wide range of fields. For example, in condensed matter systems, the finite quasiparticle lifetime caused by interactions or disorder can introduce non-Hermitian effects [5, 6]; in the system of interaction between light and medium, absorption or radiative loss in the medium can also introduce non-Hermitian terms into the wave equation [7–11]. Importantly, Non-Hermiticity enriches the manifestations of core physical concepts such as symmetry breaking and topological phase transitions. In Hermitian systems, symmetry may undergo spontaneous breaking at critical points (e.g., magnetic ordering in quantum spin systems). In contrast, the introduction of dissipation and gain in non-Hermitian systems serves as an additional tuning mechanism, thereby enabling a greater diversity of symmetry breaking phenomena. For instance, non-Hermiticity can induce the spontaneous breaking of time-reversal symmetry [12–15] or parity-time symmetry [16–19]. Meanwhile, significant progress has been made in recent years in the study of topological states of matter within non-Hermitian systems [20–22], as explored across diverse platforms including optics [23, 24], superconducting circuits [25, 26], and cold atom systems [27, 28]. Although non-Hermiticity introduces fundamental differences in aspects such as spectral structure and eigenstate orthogonality, many topological phases can still be defined and realized under appropriate frameworks of symmetry and topological classification, such as non-Hermitian versions of the Su-Schrieffer-Heeger model [29, 30], Chern insulators [31, 32], quantum spin Hall insulators [33], topological lasers [34, 35], and bulk Fermi arcs connecting exceptional points [36–38]. These emergent phenomena have profoundly expanded our understanding of the fundamental physics governing non-Hermitian and open quantum systems.

Rydberg atomic systems, leveraging their long-range interactions and high controllability [39–41], have emerged as an important experimental platform for exploring various complex quantum effects [42–45]. Through laser manipulation and tunable environmental coupling, researchers have successfully realized a series of quantum states and dynamical behaviors in Rydberg systems, such as Bose–Einstein condensation [46, 47], quantum phase transitions [48–52], topological phases [53, 54], and time crystals [55–58]. More importantly, the inherent dissipative pathways and many-body interactions in Rydberg ensembles provide a natural avenue for engineering tunable non-Hermitian Hamiltonians, thereby extending the scope of research from traditional Hermitian systems to non-Hermitian quantum physics.

In non-Hermitian Rydberg atom platforms, symmetry breaking can occur not only in static phases but can also emerge dynamically during time evolution, giving rise to phenomena such as spontaneous charge-conjugate parity or

* dds@ustc.edu.cn

particle-hole symmetry breaking [59, 60], non-Hermitian-induced complex dynamical hysteresis trajectories [59, 61], and exceptional points and their applications in enhanced sensing [60, 62, 63]. Furthermore, Rydberg atomic systems, with their highly tunable array structures, dipole exchange interactions, and close connection to quantum information processing technologies, provide a highly promising platform for realizing, tuning, and detecting topological states and non-Hermitian quantum phase transitions. Through precise design of atomic arrays [64], synthetic dimensions [65–67], and dissipative couplings [54], quantum simulators with nontrivial topological or non-Hermitian properties can be constructed in these systems, thus opening avenues for exploring frontier topics.

The integration of non-Hermitian physics with many-body systems of Rydberg atoms provides a powerful platform for exploring the non-equilibrium, non-Hermitian, and topological properties of quantum many-body physics. In this review, we primarily summarize the key experimental and theoretical advances related to Rydberg atomic systems and non-Hermitian physics. Starting from the fundamental construction of non-Hermitian Hamiltonians, we elucidate the effective dissipation mechanisms induced by Rydberg atomic interactions and analyze their impact on spectral properties and symmetry breaking. Subsequently, the emergence, dynamical behavior, and potential applications of exceptional points in quantum sensing are discussed. In addition, we outline the implementations of both topological and non-Hermitian quantum phase transitions in Rydberg atom platforms (including ensembles, synthetic dimensions, and arrays), along with a topological dissipative structure based on the Su-Schrieffer-Heeger model. These studies not only deepen the understanding of quantum phase transitions in many-body systems but also highlight the unique value of the Rydberg platform for realizing and controlling topological states.

III. NON-HERMITIAN PHYSICS

A. The basic theory of non-Hermitian systems

In quantum physics, a defining feature of non-Hermitian systems is that their eigenstates no longer satisfy orthogonality. Instead, they are characterized by a biorthonormal system, composed of left and right eigenvectors. The study of these systems is crucial for understanding a wide range of physical phenomena. These properties not only challenge the framework of traditional quantum mechanics but also provide valuable perspectives for investigating the properties of open quantum systems, dissipative phase transitions, and other key concepts. Due to $H \neq H^\dagger$ in non-Hermitian systems, it is necessary to introduce a biorthogonal basis [68]. Considering a non-Hermitian Hamiltonian

$$H_{\text{NH}} = H + i\Gamma \quad H_{\text{NH}}^\dagger = H - i\Gamma, \quad (1)$$

its eigenvalue equation can be written as

$$H_{\text{NH}}|\psi_n^R\rangle = E_n|\psi_n^R\rangle, \quad \langle\psi_n^R|H_{\text{NH}}^\dagger = E_n^*\langle\psi_n^R|, \quad (2)$$

$$H_{\text{NH}}^\dagger|\psi_n^L\rangle = E_n^*|\psi_n^L\rangle, \quad \langle\psi_n^L|H_{\text{NH}} = E_n\langle\psi_n^L|. \quad (3)$$

E_n and E_n^* are the corresponding eigenvalues, where n is the index used to distinguish the eigenvalues. If the eigenvalues of the Hamiltonian are non-degenerate, then although the eigenspace of the Hamiltonian is complete, the eigenstates do not satisfy orthonormality. For two right eigenstates $|\psi_m^R\rangle$ and $|\psi_n^R\rangle$, based on $2H = H_{\text{NH}} + H_{\text{NH}}^\dagger$ and $2i\Gamma = H_{\text{NH}} - H_{\text{NH}}^\dagger$, we obtain

$$\langle\psi_m^R|2H|\psi_n^R\rangle = \langle\psi_m^R|(H_{\text{NH}} + H_{\text{NH}}^\dagger)|\psi_n^R\rangle = (E_n + E_m^*)\langle\psi_m^R|\psi_n^R|\psi_m^R|\psi_n^R\rangle, \quad (4)$$

$$\langle\psi_m^R|2i\Gamma|\psi_n^R\rangle = \langle\psi_m^R|(H_{\text{NH}} - H_{\text{NH}}^\dagger)|\psi_n^R\rangle = (E_n - E_m^*)\langle\psi_m^R|\psi_n^R|\psi_m^R|\psi_n^R\rangle, \quad (5)$$

$$\langle\psi_m^R|\psi_n^R|\psi_m^R|\psi_n^R\rangle = 2\frac{\langle\psi_m^R|H|\psi_n^R\rangle}{E_m^* + E_n} = 2i\frac{\langle\psi_m^R|\Gamma|\psi_n^R\rangle}{E_n - E_m^*} \neq 0. \quad (6)$$

This indicates that different right eigenstates are non-orthogonal. However, by introducing the biorthogonal basis

$$\langle\psi_m^L|H_{\text{NH}}|\psi_n^R\rangle = E_n\langle\psi_m^L|\psi_n^R|\psi_m^L|\psi_n^R\rangle = E_n\langle\psi_m^L|\psi_n^R|\psi_m^R|\psi_n^R\rangle, \quad (7)$$

we find that if $E_m \neq E_n$, then $\langle\psi_m^L|\psi_n^R|\psi_m^L|\psi_n^R\rangle$ must equal zero. For a general non-Hermitian Hamiltonian, its eigenvalues are typically complex unless specific symmetries are present. If the left and right eigenstates are linearly independent, they can be biorthogonalized

$$|\tilde{\psi}_n^R\rangle = \frac{|\psi_n^R\rangle}{\sqrt{\langle\psi_n^L|\psi_n^R|\psi_n^L|\psi_n^R\rangle}}, \quad |\tilde{\psi}_n^L\rangle = \frac{|\psi_n^L\rangle}{\sqrt{\langle\psi_n^L|\psi_n^R|\psi_n^L|\psi_n^R\rangle}}. \quad (8)$$

The biorthogonalized eigenstates satisfy the following orthonormality and completeness relations

$$\langle \tilde{\psi}_m^L | \tilde{\psi}_n^R \rangle \langle \tilde{\psi}_m^L | \tilde{\psi}_n^R \rangle = \delta_{mn}, \quad \sum_n \langle \tilde{\psi}_n^R \rangle \langle \tilde{\psi}_n^L \rangle = \mathbb{I}. \quad (9)$$

At present, the physical realization of non-Hermitian systems primarily relies on two mechanisms: non-reciprocal coupling and gain or loss. In lattice models, non-reciprocal coupling manifests as the non-reciprocity of hopping amplitudes between adjacent sites, meaning that the coupling strength from site j to site $j+1$, denoted as t_{jL} , is not equal to the reverse coupling t_{jR} [69], leading to the directional transport of energy or particle flow. On the other hand, the gain and loss mechanism corresponds to introducing a complex on-site potential at each lattice site, where the imaginary part represents gain (positive imaginary part) or loss (negative imaginary part) [70]. This is often achieved in practical systems through optical pumping, radiative decay, or coupling to external environments.

Precise control of non-reciprocal coupling typically requires specially designed temporal modulation or nonlinear components, making it relatively challenging to implement. In contrast, gain and loss are more commonly encountered in open systems such as photonic [71, 72], acoustic [73, 74], and cold atom platforms [19, 75]. Furthermore, by spatially engineering the distribution of dissipation, gain-loss structures can be effectively constructed [3, 76]. Therefore, studying non-Hermitian systems from the perspective of gain and loss not only offers greater experimental feasibility but also provides a practical framework for exploring Non-Hermitian physics in a wide range of open systems.

B. Symmetry in non-Hermitian systems

Symmetry and its breaking are central to understanding phase transitions and the classification of quantum states in many-body systems [77, 78]. The most fundamental symmetry is internal (non-spatial) symmetry, which does not depend on any specific spatial structure. Within Hermitian systems, the key internal symmetries are formalized by the Altland-Zirnbauer classification [79]: time-reversal symmetry, particle-hole symmetry [80], and chiral symmetry.

In non-Hermitian systems, symmetry continues to play a crucial role in governing topological phases. A principal distinction between Hermitian and non-Hermitian systems lies in their accessible degrees of freedom. Non-Hermitian systems can realize non-unitary operations that are forbidden in Hermitian contexts. This ability allows the energy spectrum to shift from the real axis to the complex plane, thereby expanding the parameter space needed to describe the system. As a result, the study of symmetry in non-Hermitian physics not only generalizes Hermitian topological concepts but also predicts the emergence of topological phases. Indeed, non-Hermiticity fundamentally splits and unifies symmetry. To illustrate symmetry splitting, we take particle-hole symmetry as an example. In a Hermitian system, particle-hole symmetry is defined as [2]

$$\mathcal{C}H^*\mathcal{C}^{-1} = -H, \quad (10)$$

where \mathcal{C} is a unitary matrix. For non-Hermitian systems, however, $H^* \neq H^T$ (where H^* denotes the complex conjugate of the Hamiltonian, and H^T denotes the transpose of the Hamiltonian); therefore, the above definition is not equivalent to the one based on transposition [2]:

$$\mathcal{C}H^T\mathcal{C}^{-1} = -H. \quad (11)$$

Therefore, Eq. 11 is used to describe the particle-hole symmetry in non-Hermitian systems.

Similarly, in non-Hermitian systems, chiral symmetry includes [2]:

$$\Gamma H \Gamma^{-1} = -H, \quad (12)$$

$$\Gamma H^\dagger \Gamma^{-1} = -H, \quad (13)$$

where Γ is a unitary matrix. In addition, time-reversal symmetry is an independent symmetry class in one-dimensional Hermitian systems, satisfying [3]:

$$\mathcal{T}H^*\mathcal{T}^{-1} = H, \quad (14)$$

where $\mathcal{T} = U_{\mathcal{T}}\mathcal{K}^*$ is a unitary matrix, and \mathcal{K}^* is a complex conjugate operation. Furthermore, the time-reversal symmetry in non-Hermitian systems is expressed as [3]:

$$\mathcal{T}H^T\mathcal{T}^{-1} = H. \quad (15)$$

Table I. In the presence of symmetry, the properties of eigenvalues E_i for 2×2 and 3×3 non-Hermitian matrices (Table adapted from Ref. [81]). PT denotes parity-time symmetry and CP denotes charge-conjugate parity symmetry. Degree n denotes the dimension of the system Hamiltonian, and $\text{sgn } \Delta$ indicates symmetry ($\Delta = +1$) and symmetry breaking ($\Delta = -1$).

Degree n	$\text{sgn } \Delta$	PT	CP
2	+1	$E_i \in \mathbb{R}, E_1 \neq E_2$	$E_1 = -E_2^*$
	0	$E_1 = E_2$	$E_1 = E_2$
	-1	$E_1 = E_2^*$	$E_i \in i\mathbb{R}, E_1 \neq E_2$
3	+1	$E_i \in \mathbb{R}, E_1 \neq E_2 \neq E_3$	$E_1 = -E_2^* \text{ and } E_3 \in i\mathbb{R}$
	0	$E_1 = E_2 \text{ and } E_3 \in \mathbb{R}$	$E_1 = E_2 \text{ and } E_3 \in i\mathbb{R}$
	-1	$E_1 = E_2^* \text{ and } E_3 \in \mathbb{R}$	$E_i \in i\mathbb{R}, E_1 \neq E_2 \neq E_3$

Beyond the conventional internal symmetries previously discussed, certain non-Hermitian systems also exhibit parity-time symmetry. Initially introduced in theoretical studies, parity-time symmetric non-Hermitian systems allow for entirely real spectra. For a Hamiltonian $H(r, p, t)$, where r , p , and t denote the position, momentum, and time, respectively. If H is a parity-time symmetric Hamiltonian, then it satisfies the commutation relation $[H, \text{PT}] = 0$ (PT is the combined parity and time reversal operator). Here, the parity operator P performs a spatial reflection, transforming $r \rightarrow -r$ and $p \rightarrow -p$. The time reversal operator T reverses the direction of time, mapping $t \rightarrow -t$ and simultaneously flipping the sign of momentum, $p \rightarrow -p$. In particular, the emergence of a phase transition point breaks the symmetry, leading to the spontaneous breaking of parity-time symmetry beyond this point. Such a phase transition point is typically an exceptional point, where the system's eigenenergies and eigenstates coalesce simultaneously. After traversing the exceptional point, the system generates symmetric and symmetry-broken phases. In the parity-time symmetric phase, the eigenvalues have distinct real parts but degenerate imaginary parts. Conversely, in the parity-time broken phase, the real parts become degenerate while the imaginary parts split. Recently, charge-conjugate parity symmetry has also been identified in non-Hermitian systems [59, 81]. A non-Hermitian Hamiltonian with parity-time symmetry protection maintains a purely real energy spectrum, whereas the behavior of energy spectra under charge-conjugate parity symmetry is more complex. Researchers have characterized the energy spectra of systems with parity-time and charge-conjugate parity symmetry or their breaking, as shown in Table I.

C. Topological properties of the non-Hermitian systems

The topological phenomena emerging in non-Hermitian systems are indeed more diverse and abundant compared to traditional Hermitian systems. The core difference lies in the complex eigenvalues of the non-Hermitian system, which directly introduces new dimensions and symmetry requirements, thereby giving rise to a large number of abundant phenomena. Therefore, topological phases have been a major focus of research, particularly regarding their distinctive characteristics. Generally, the complex energy plane used to describe topological properties includes two types of complex energy gaps [2]: point gap [Fig. 1(a) Upper plane] and line gap [Fig. 1(a) Lower plane]. In the presence of a point (line) gap, complex energy bands do not cross a reference point (line) in the complex energy plane. Physically, point gaps are relevant to localization transitions in one-dimensional non-Hermitian systems, whereas topologically protected edge states are often explained via line gaps in the real part of the spectrum [84, 85].

A non-Hermitian Hamiltonian H is defined to have a point gap when its complex plane spectrum avoids a reference point $E_B \in \mathbb{C}$, i.e., $\det(H - E_B) \neq 0$. The simplest nontrivial example of the point gap topological phases appears in one-dimensional systems. Whereas $\det(H - E_B)$ is always real for Hermitian H , it can be complex for non-Hermitian H . This leads to the following definition of the winding number $W(E)$ [86]:

$$W(E) = \int_0^{2\pi} \frac{dk}{2\pi i} \frac{d}{dk} \log \det(H(k) - E_B) \quad (16)$$

where $H(k)$ is the non-Hermitian Bloch Hamiltonian in momentum space with a finite number of bands ($k \in [0, 2\pi]$). The topological properties of point gap spectra are usually characterized by non-zero winding numbers $W(E) \neq 0$.

Non-Hermitian systems also exhibit a range of fascinating phenomena, such as exceptional points in the energy spectrum and the non-Hermitian skin effect. Exceptional points represent a special type of degeneracy where not only do the eigenvalues (both real and imaginary parts) coalesce, but the corresponding eigenvectors also become fully parallel. Near exceptional points, the eigenvalues exhibit extremely high sensitivity to small variations in system parameters. In the simplest two mode system, a perturbation parameter ε to the Hamiltonian can induce eigenfrequency shifts on the order of $\sqrt{\varepsilon}$. This $\sqrt{\varepsilon}$ -scaling suggests a greatly enhanced response for small ε , paving the way for applications in ultrasensitive sensing [87–90]. Moreover, in the steady-state regime, dynamically encircling

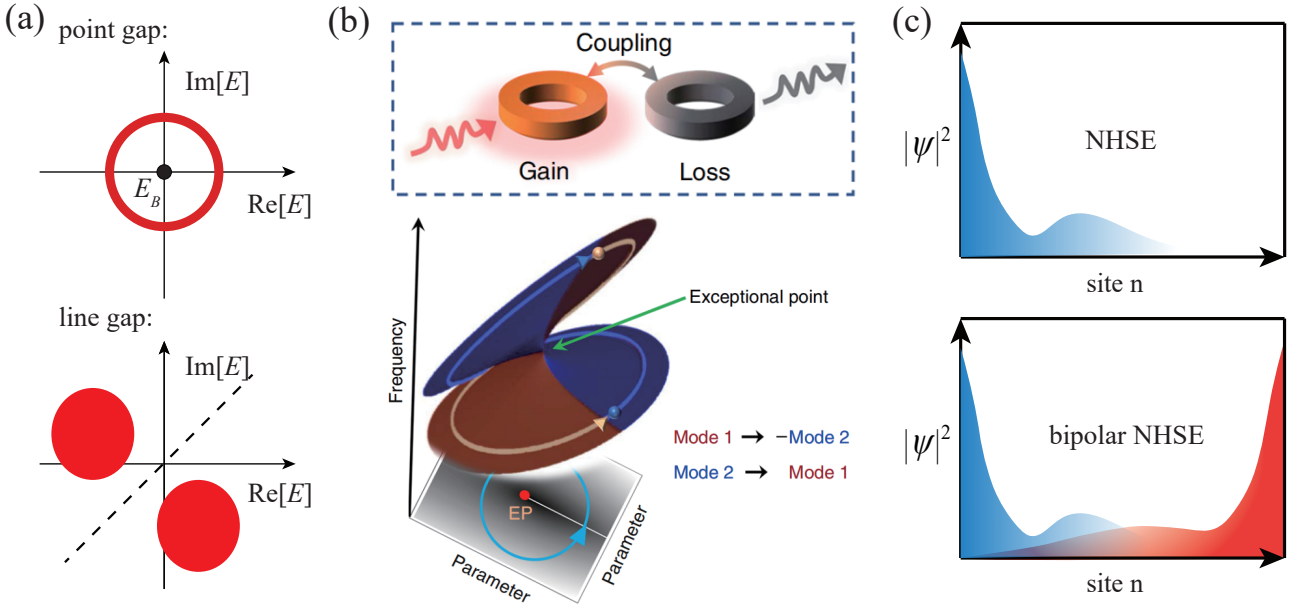


Figure 1. (a) On the complex spectral plane, non-trivially encircle nonzero areas and form the so-called point gaps, or may eigenbands (red) may be separated by line gaps, thereby leading to much richer symmetry-protected topological states (Figure adapted from Ref. [82]). (b) a universal photonic non-Hermitian system consists of coupled gain and loss materials, such as a ring resonator (inset in Figure A). Under certain critical coupling values and gain/loss coefficients, exceptional points may occur in the frequency spectrum of such systems. The topological properties of a second-order exceptional point are best understood by two Riemann surfaces (shown in blue and brown colours) connected at the square root branch point. Starting on the upper surface, one ends up on the lower surface after one round and vice versa (the states move smoothly from one surface to the other). Encircling twice brings one back to the initial point, but the modes acquire a π -Berry phase; after 4 cycles, the modes return to their starting phases (Figure adapted from Ref. [83]). (c) All eigenstates are localized at the system boundary in an exponentially decaying manner, which is the non-Hermitian skin effect.

a second-order Exceptional point over a full cycle results in eigenstate exchange accompanied by the acquisition of a π Berry phase [83]. This behavior originates directly from the topological structure associated with exceptional points in the complex eigenvalue spectrum (Fig. 1(b)). Another remarkable phenomenon in non-Hermitian and open quantum systems is the non-Hermitian skin effect, which describes the localization of eigenstates at boundaries [91–93], as illustrated in Fig. 1(c). The non-Hermitian skin effect plays a vital role in understanding topological phases in non-Hermitian systems [94, 95]. Recent studies have extended the concept to more complex manifestations such as the bipolar non-Hermitian skin effect [96, 97] and the many-body critical non-Hermitian skin effect [98, 99], which hold promise for applications in optical devices and quantum information technologies.

D. Lindblad master equation

Under the Markov approximation, open systems quantum dynamics are described by the Lindblad master equation [100]:

$$\dot{\rho} = -i[H, \rho] + \sum_j \left(L_j \rho L_j^\dagger - \frac{1}{2} \{ L_j^\dagger L_j, \rho \} \right), \quad (17)$$

where ρ denotes the system's density matrix, H represents the Hermitian Hamiltonian, and L_j is the jump operator. This can be written compactly as $d\rho(t)/dt = \mathcal{L}\rho(t)$, with \mathcal{L} denoting the Liouvillian superoperator, a non-Hermitian operator that effectively governs the non-unitary evolution of the density matrix. By introducing the effective non-Hermitian Hamiltonian $H_{\text{NH}} = H - \frac{i}{2} \sum_j L_j^\dagger L_j$, the master equation takes the form [100]:

$$\frac{\partial}{\partial t} \rho = -i (H_{\text{NH}} \rho - \rho H_{\text{NH}}^\dagger) + \sum_j L_j \rho L_j^\dagger. \quad (18)$$

Here, the first two terms capture the non-unitary evolution generated by H_{NH} , while the last term represents quantum jumps due to environmental coupling. On time scales shorter than the typical interval between quantum jumps, the dynamics are approximately governed by H_{NH} alone. In this regime, a pure state evolves as $\partial_t |\psi\rangle = -iH_{\text{NH}}|\psi\rangle$. As time evolves, there is a finite probability of a quantum jump occurring, producing a new state $|\psi(t)\rangle \rightarrow L_j|\psi(t)\rangle$. Subsequently, this state continues to evolve under H_{NH} until the next quantum jump occurs. This process defines a quantum trajectory of the state $|\psi\rangle$ driven jointly by the non-Hermitian effective Hamiltonian and the quantum jumps.

Experimentally, measurement devices can respond to whether the quantum transition occurs or not, and then select a certain quantum trajectory according to the measurement result, which corresponds to the post selection. Since the density matrix can be regarded as the superposition of many pure states, the evolution of the density matrix under the Lindblad quantum master equation can be obtained by summing all possible quantum trajectories. Consequently, the study of open quantum systems centers on two key non-Hermitian operators: H_{NH} , describing the time evolution of the wave function under post selection, and \mathcal{L} , describing the time evolution of the density matrix.

E. Liouvillian exceptional point in open system

In quantum open systems, exceptional points also appear in the Liouvillian spectrum, which is described by the evolution of the density matrix driven by the Liouvillian operator [101, 102]. Hui-Xia Gao et al. utilized the flexible control characteristics of single-photon interferometry to thoroughly investigate the phenomenon of chiral state transfer when the Liouvillian exceptional point is parametrically encircled [103]. The study reveals that the chirality of the dynamics only manifests within an intermediate timescale for encircling and is governed by the structure of the Liouvillian spectrum near the exceptional point. Importantly, the evolutionary trajectory generated by encircling an exceptional point exhibits similarities to the features presented in the Liouvillian spectrum diagram and the Riemann surface of the non-Hermitian Hamiltonian. Additionally, their findings reveal that over longer time scales, the system will relax to a steady state, with the chirality disappearing and becoming independent of the direction of parametric encircling. The experiment explicitly confirms the existence of chiral state transfer near the Liouvillian exceptional point, revealing its transient characteristics and laying the foundation for future exploration of the rich physical implications of Liouvillian exceptional points in open quantum systems.

This study takes an open system containing two energy levels $\{|0\rangle, |1\rangle\}$ as an example, and its hybrid Lindblad master equation can be described as [103]:

$$\dot{\rho} = -i(H\rho - \rho H^\dagger) + L_\phi \rho L_\phi^\dagger - \frac{1}{2} L_\phi^\dagger L_\phi \rho - \frac{1}{2} \rho L_\phi^\dagger L_\phi := \mathcal{L}\rho, \quad (19)$$

where \mathcal{L} is a Liouvillian superoperator, and the non-Hermitian Hamiltonian is given by $H = H_0 - i\Gamma|1\rangle\langle 1|$,

$$H_0 = \begin{pmatrix} \frac{\delta_1}{2} & -\Omega_1 \\ -\Omega_1^* & -\frac{\delta_1}{2} \end{pmatrix}. \quad (20)$$

The dephasing channel is characterized by the quantum jump operator $L_\phi = \sqrt{\gamma_\phi}|1\rangle\langle 1|$ with the dephasing rate γ_ϕ . The Liouvillian eigenspectrum λ_i is calculated through $\mathcal{L}\rho_i^R = \lambda_i\rho_i^R$ with the corresponding Liouvillian eigenstates ρ_i^R . Exceptional points can also arise in the Liouvillian eigenspectrum with coalescing eigenenergies and eigenstates.

IV. NON-HERMITIAN PROPERTIES IN RYDBERG ATOM SYSTEMS

Rydberg atom systems provide a highly controllable platform for studying non-Hermitian physics, where many-body interactions naturally introduce effective dissipation channels [39, 41, 104]. One prominent mechanism arises from the long-range interactions between atoms excited to Rydberg states. When multiple atoms occupy Rydberg levels, exchange and collision processes lead to dissipation, which effectively generates non-Hermitian characteristics. This dissipation also arises from the Rydberg blockade effect: once an atom is excited to a Rydberg state, it suppresses further excitations within a characteristic blockade radius around it, forming a collective excitation known as a Rydberg polariton [105, 106]. The spatial inhomogeneity of such polaritons gives rise to position-dependent phase shifts, which effectively accelerate the decay of Rydberg state populations and produce energy dissipation throughout the ensemble. These interaction-induced dissipative processes enable the realization of a tunable non-Hermitian Hamiltonian in Rydberg systems, thereby facilitating investigations into exceptional points, symmetry breaking, non-equilibrium dynamics, and topological phenomena in open quantum systems [54, 59–63].

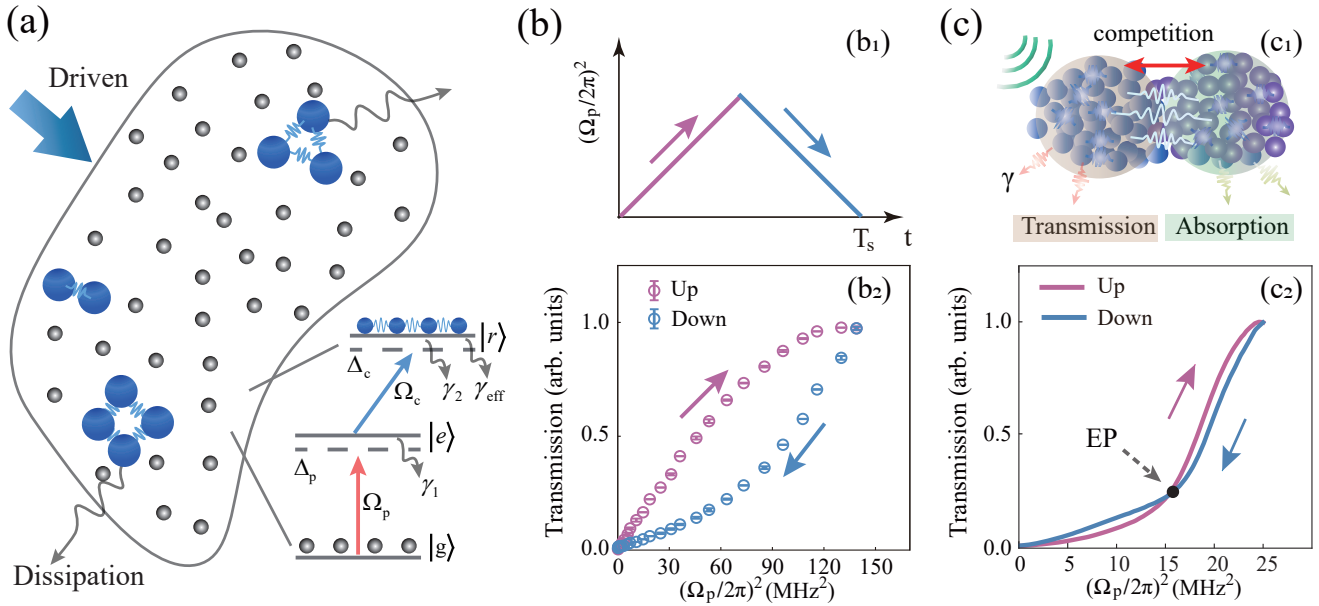


Figure 2. Schematic of many-body interaction induced hysteresis loops in Rydberg atoms. (a) Rydberg atomic energy level diagrams. Probe Ω_p and coupling Ω_c fields excite atoms with detunings Δ_p and Δ_c . γ_1 and γ_2 are decay rates of states $|e\rangle$ and $|r\rangle$, and γ_{eff} is the decay rate caused by Rydberg many-body interactions. (b) Measured transmission by positively (Up, pink) and negatively (Down, blue) scanning $(\Omega_p/2\pi)^2$ in (b₁), the trajectories connected by data points exhibit hysteresis loop in (b₂) (Figure adapted from Ref. [59]). (c) The atomic system in (c₁) and hysteresis trajectory in (c₂) after adding microwaves field (Figure adapted from Ref. [60]).

A. Non-Hermitian hysteresis trajectories induced by many-body interactions

Based on the three-level Rydberg atomic system shown in Fig. 2(a), the system consists of three atomic manifolds: the ground state $|g\rangle$, metastable state $|e\rangle$, and Rydberg state $|r\rangle$. The probe field drives the transition $|g\rangle \rightarrow |e\rangle$ with Rabi frequency (detuning) Ω_p (Δ_p), while the coupling field drives the transition $|e\rangle \rightarrow |r\rangle$ with Rabi frequency (detuning) Ω_c (Δ_c). The spontaneous decay rates of states $|e\rangle$ and $|r\rangle$ are denoted by γ_1 and γ_2 , respectively, and γ_{eff} represents the effective decay rate induced by Rydberg many-body interactions. For a pair of atoms i and j located at positions r_i and r_j , when both are excited to the Rydberg state $|r\rangle$, they interact via a van der Waals (vdW) potential given by $V_{\text{vdW}} \propto C_6/R^6$, where C_6 is the dispersion coefficient and $R = |r_i - r_j|$ is the distance between the two Rydberg atoms. Under the rotating-wave approximation, the Hamiltonian of the system can be written as [59]:

$$H_{\text{many}} = \sum_{j=1}^N \left[-(\Delta_p + \Delta_c) \hat{\sigma}_{rr}^j - (\Omega_p \sigma_{eg}^j + \Omega_c \sigma_{re}^j + \text{H.c.}) \right] + \sum_{j=1}^N \left[-\Delta_p \hat{\sigma}_{ee}^j + \sum_{j < k} V_{jk} \sigma_{rr}^j \sigma_{rr}^k \right], \quad (21)$$

where $\sigma_{\alpha\beta}^j = |\alpha_j\rangle\langle\beta_j|$ ($\alpha, \beta = e, g, r$).

In the mean-field approximation, a single atom is considered to experience an effective field resulting from its interactions with all other atoms. Consequently, the problem of solving the dynamic many-body system is reduced to addressing the dynamics of a single atom within the effective field, while the other atoms are treated as part of the environment. In the following treatment, the reduced density matrix of the single atom system is used, and the non-Hermitian Hamiltonian is given by [59]:

$$H_1 = -\Delta_p \hat{\sigma}_{ee} - (\Delta_p + \Delta_c - \frac{i\gamma_{\text{eff}}}{2}) \hat{\sigma}_{rr} - (\Omega_p \sigma_{eg} + \Omega_c \sigma_{re} + \text{H.c.}), \quad (22)$$

where γ_{eff} reveals the effective decay rate induced by the interaction with the environment. When $\Delta_p = \Delta_c = 0$,

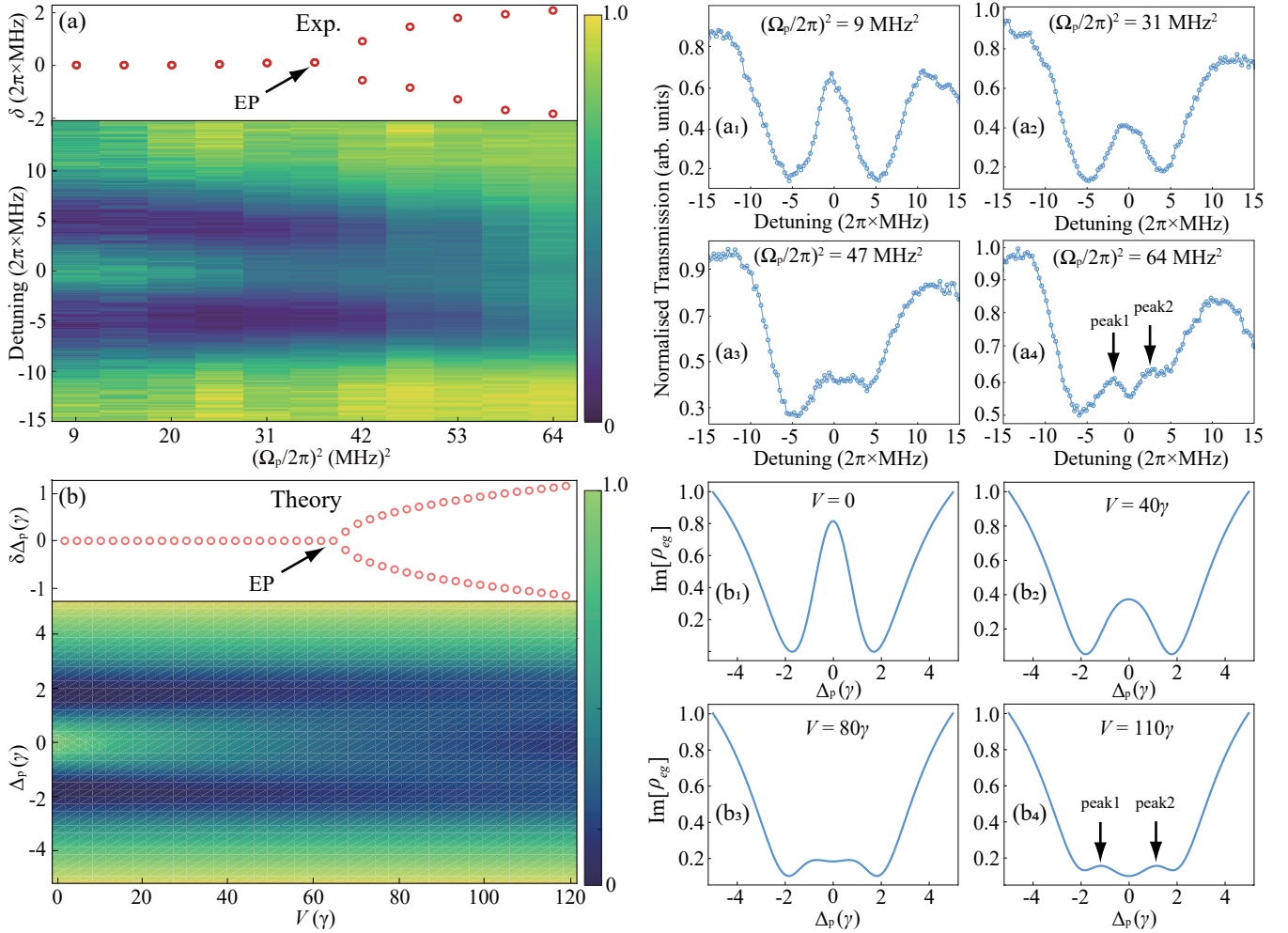


Figure 3. Measured phase diagram and theoretical phase diagram (Figure adapted from Ref. [59]). (a) The measured phase diagram versus the probe intensity $(\Omega_p/2\pi)^2$ and detuning Δ_p . (a₁)-(a₄) The measured electromagnetically induced transparency spectrum varies with the intensity of the probe field. (b) Theoretical spectrum $\text{Im}[\rho_{eg}]$ versus the interaction strength V and detuning Δ_p . With further increase in interaction strength, the system transits an exceptional point (marked by the black arrow in the up panel of (b)). As the interaction strength V gradually increases, the spectrum $\text{Im}[\rho_{eg}]$ as shown in (b₁)-(b₄).

the non-Hermitian Hamiltonian is charge-conjugate parity symmetric, and it satisfies $U_{CP}H_1U_{CP}^{-1} = -H_1^*$ with $U_{CP} = \text{diag}(1, -1, 1)$ [59, 81].

Jun Zhang et al. have experimentally observed non-Hermitian hysteresis trajectories in a three level Rydberg atomic many-body system [59], as shown in Fig. 2(b₂). The study found that the hysteresis trajectories formed during the upward and downward scans of the probe field do not coincide, indicating the presence of interaction-induced dissipation in the system. Additionally, their study also demonstrates that introducing microwave field control to the three-level Rydberg atomic system leads to intersecting hysteresis trajectories, as illustrated in Fig. 2(c₂). This occurs because the introduction of the microwave field breaks the original three level structure, and the resulting four level system satisfies particle-hole symmetry. When the probe field scans past the exceptional point, the symmetry of the system is spontaneously broken, and the spectrum transitions from transmission to absorption, generating intersecting trajectories.

B. Exceptional points in cold Rydberg atomic gases

Recent studies have shown that open systems undergo phase transitions at exceptional points, leading to a variety of interesting physical phenomena, including chirality [107, 108], unidirectional transmission or reflection [109, 110], topological phase transitions [111, 112], symmetry breaking [18, 81, 113], and high sensitivity detection [114, 115].

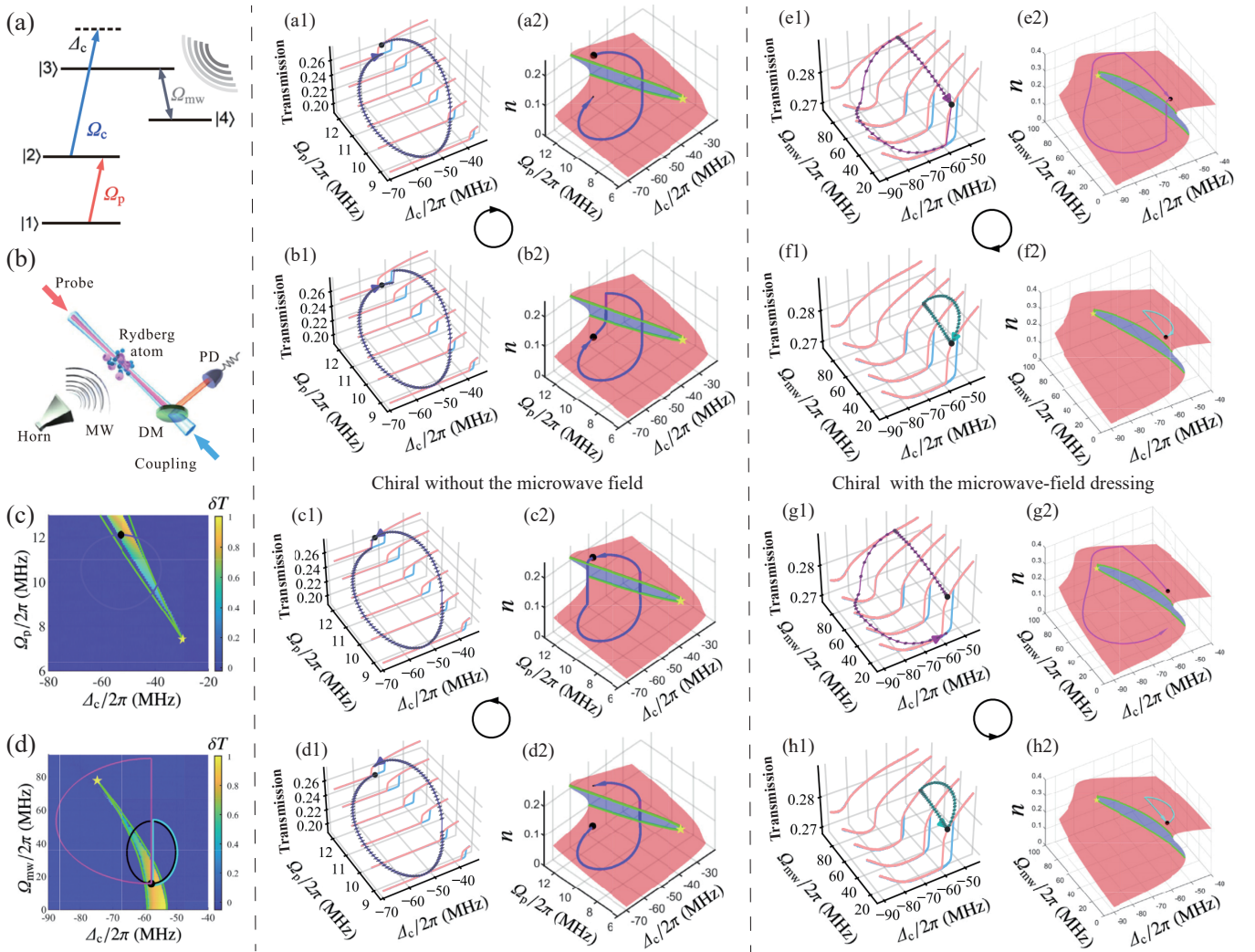


Figure 4. Exceptional structures in a thermal Rydberg gas and the measured chiral mode (Figure adapted from Ref. [61]). (a) Schematics of the coupling scheme. (b) Experimental setup. (c)-(d) Experimentally measured phase diagrams. The color bar represents the normalized transmission difference, δT between the forward and backward scans of Δ_c . The green lines represent the numerically fitted second-order exceptional lines, and the yellow star is the third order exceptional point. (a1-d1) Chiral mode switching without the microwave field. (a2-d2) The corresponding numerically calculated encircling trajectories on the landscape of the steady-state Rydberg population. (e1-h1) Chiral mode switching with the microwave-field dressing. (e2-h2) The corresponding numerically calculated encircling trajectories on the landscape of the steady-state Rydberg population.

These properties have become the focus of research on non-Hermitian systems related to exceptional points, driving a series of experimental studies in optics, electronics, and cold atomic physics. The combination of non-Hermitian properties and many-body interactions makes the emergence of non-trivial effects possible, thus providing a platform for the study of emerging phases.

Jun Zhang et al. experimentally demonstrated the emergence of exceptional points and associated spectral bifurcations in cold Rydberg atomic gases [59]. By measuring the transmission spectrum as a function of probe detuning Δ_p and intensity $(\Omega_p/2\pi)^2$, a phase diagram was mapped, revealing the process of crossing the exceptional point as the probe field intensity increases [Fig. 3(a)]. Under weak probe intensity, the system exhibits a conventional electromagnetically induced transparency spectrum [Fig. 3(a1)]. As the probe intensity increases, interactions between Rydberg atoms are enhanced, resulting in stronger dissipation. Consequently, the electromagnetically induced transparency peak weakens [Fig. 3(a3)], and eventually splits into two distinct peaks at higher intensities [Fig. 3(a4)], signifying the crossing of a second-order exceptional point. The peaks in Fig. 3(a4) are asymmetric due to the small shift in the Rydberg energy level. Moreover, the observed splitting beyond the exceptional point serves as a signature of the breaking of charge-conjugate parity symmetry [81].

Theoretically, by solving the master equation Eq. 17 under steady state conditions $\dot{\rho} = 0$, they simulated the

spectrum of $\text{Im}[\rho_{eg}]$ as a function of interaction strength V and the detuning Δ_p [Fig. 3(b), lower panel]. Similar to the experimental observations, as the interaction V increases from $V = 0$ to $V = 110\gamma$, the peak of $\text{Im}[\rho_{eg}]$ decreases, and two peaks emerge, as illustrated in Figs. 3(b₁)-(b₄) and the upper panel of Fig. 3(b). During this process, the system passes through exceptional points, and the peak of $\text{Im}[\rho_{eg}]$ splits into two, indicating that a degenerate complex eigenvalue of the system has become non-degenerate.

C. Chiral switching of many-body steady states in a dissipative Rydberg gas

Non-Hermitian physics provides a unique perspective and insights into exploring the non-equilibrium dynamics of dissipative Rydberg gases. Chong-Wu Xie et al. experimentally observed the chiral switching of many-body steady states in dissipative hot Rydberg vapors [61]. These phenomena are similar to the typical chiral state transfer observed in non-Hermitian systems [101, 102, 116]. This research reveals that the existence of both bistability and chiral dynamics originate from the Liouvillian exceptional structure, where two exceptional lines merge at a higher-order exceptional point. As parameters undergo adiabatic variation along a closed path, the Rydberg gas can switch between two distinct collective steady states characterized by different Rydberg excitations and optical transmissions. From the perspective of non-Hermitian physics, dissipative Rydberg gases establish a paradigm for chiral mode switching via parameter tuning and open up application avenues based on unique non-Hermitian properties.

Similar to the formation of exceptional point rings in non-Hermitian physics [117], the choice of the initial state is crucial for observing chiral mode switching. In this experiment, the authors initialize the system in a steady state within the bistable region and slowly vary it along the purple loop shown in Fig. 4(c) without the microwave field dressing and in Fig. 4(d) with the microwave field dressing. Figures 4(a1) and (c1) show the measured transmittance when the system is initialized in a high-energy steady state without microwave dressing. When the parameters are varied clockwise, the measured transmittance decreases upon returning to the initial point, indicating a state switch. Conversely, when the parameters are rotated counterclockwise, the measured transmittance returns to its initial value, and the system reverts to the original steady state. As illustrated in Figs. 4(b1) and (d1), when the system is initialized in a low-energy steady state, the chirality of the state switching is reversed. In the case of microwave dressing, richer chiral switching phenomena are demonstrated in Figs. 4(e1)-(h1), with all theoretical simulation results presented in Figs. 4(a2)-(h2).

D. Controlling Rydberg atom-polariton interactions: from exceptional points to fast readout

The long-range interactions and tunability of Rydberg atoms have become the foundation for many frontier fields, such as quantum computing, simulation, and sensing. When coupled with the photons propagating in the atomic cloud, they can achieve optical nonlinear effects, forming collective atomic excitation states known as Rydberg polaritons. These polaritons have strong interactions with each other. Tamara Šumarač et al. experimentally investigated the interactions between Rydberg polaritons in an atomic ensemble and a neighboring individual Rydberg atom [62], revealing three distinct quantum dynamical regimes of transmission: polariton blockade, coherent exchange, and probabilistic hopping. The exceptional point acts as the critical transition between the polariton blockade and coherent exchange mechanisms. This research reveals the physical mechanism of the dipole interaction between Rydberg atoms and polaritons, laying the foundation for readout techniques based on ensembles in neutral atomic quantum processors and nonlinear photon networks for photon quantum random walks [118].

As shown in Fig. 5(a), the contrast exhibits clear piecewise characteristics with the variation of the atom-polariton distance. Meanwhile, the eigenvalue calculations of a non-Hermitian Hamiltonian in Fig. 5(b) reveal an exceptional point emerging between the blockade and coherent exchange regimes. Furthermore, the authors utilized Rydberg atom-polariton interactions to conduct experiments on fast, remote, and non-destructive qubit readout. Figure 5(c) presents the results of a single-shot detection of a Rydberg atom, achieving a fidelity of 47(5)%. Figure 5(d) also shows that repeated detection improved the fidelity to 79(4) %. Additionally, Figures 5(e) and (f) demonstrate the capability of this remote detection method for state-selective and remote detection of a single Rydberg qubit over a distance of 20 μm . After applying a global microwave field drive, long-lived and coherent microwave Rabi oscillations were observed, confirming the practical applicability of this approach.

V. SENSING BASED ON EXCEPTIONAL POINTS IN THE RYDBERG ATOMIC SYSTEM

Rydberg atoms excited to high energy levels possess characteristics such as strong polarizability and significant electric dipole moments, making them highly sensitive probes for detecting electric fields [119–121]. Currently, microwave

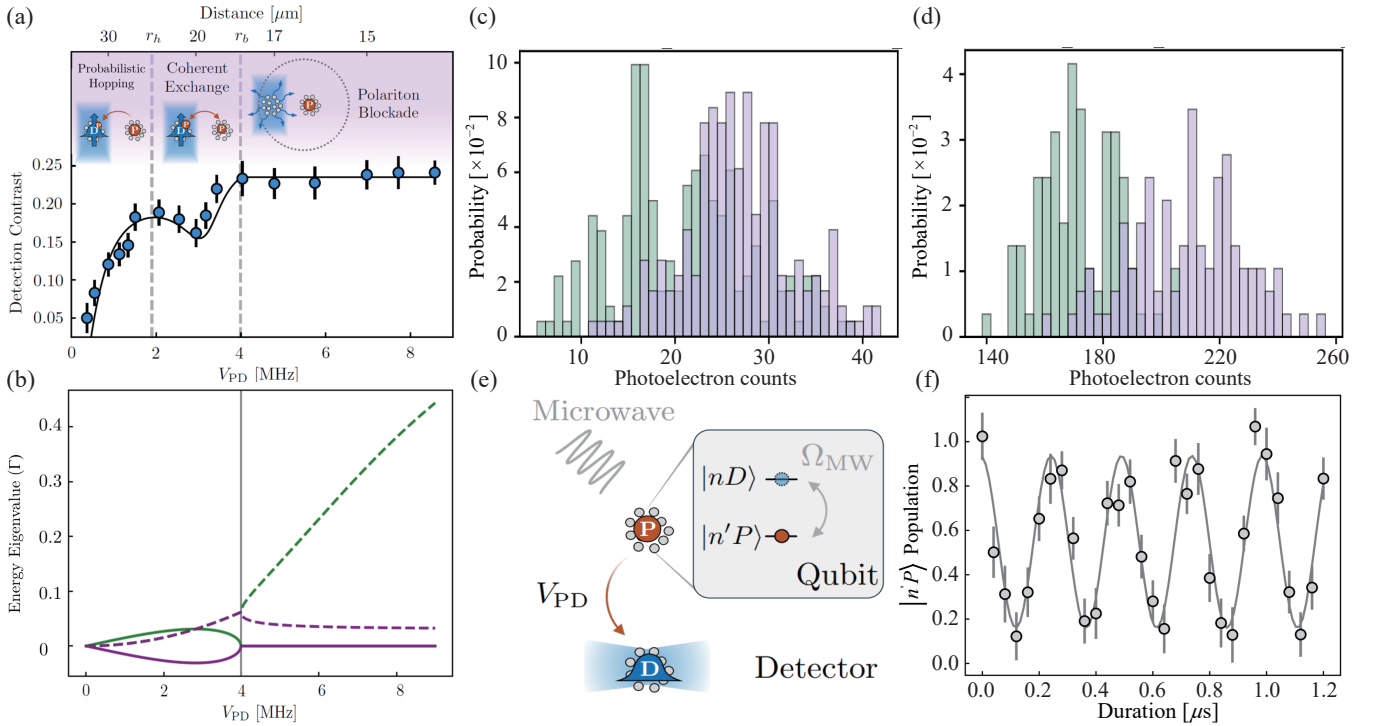


Figure 5. Rydberg electromagnetically induced transparency as a remote detector of single Rydberg atoms (Figure adapted from Ref. [62]). (a) Three distinct regimes, corresponding to probabilistic hopping, coherent exchange, and polariton blockade, can be identified. (b) The real (solid) and imaginary (dashed) parts of the eigenvalues as a function of the dipole-dipole interaction strength, V_{PD} . An exceptional point clearly emerges at the interaction strength corresponding to the blockade radius (gray line). (c) Single-shot histogram for 30 μ s of readout, showing the difference in detected photons exiting the detector ensemble with (green) and without (purple) a Rydberg atom nearby. The measurement fidelity is 47(5) %. (d) Using repeated preparation and detection (20 repetitions of 10 μ s detection), we achieve a fidelity of 79(4) %. (e) Detection schematic diagram. (f) Following a global microwave drive, state-selective and remote detection of the Rydberg qubit is performed, showing long-lived coherent microwave Rabi oscillations.

detection technology based on Rydberg atoms has become a frontier in the field of quantum precision measurement [122, 123]. Early experiments achieved high-precision measurement of microwave electric fields by combining electromagnetically induced transparency with the Autler-Townes effect [124, 125]. Dong-Sheng Ding et al. also utilized the Rydberg atomic system to achieve high sensitivity measurements from single-body to many-body phase transitions [52]. More recently, dissipative Rydberg atom systems exhibiting non-Hermitian properties have been shown to offer significant advantages for microwave detection [60, 63]. In particular, sensing enhanced by exceptional points in non-Hermitian systems has been demonstrated across various platforms, including optical cavities [90, 126], photonic crystals [127], circuit systems [128, 129], and atomic systems [130]. By leveraging a non-Hermitian Rydberg atomic platform, Ya-Jun Wang et al. achieved a significant enhancement in sensitivity by utilizing the nonlinear effects generated through microwave manipulation of exceptional points [60]. In a parallel approach, Chao Liang et al. focused on a different mechanism: they leveraged the square-root amplification of perturbations near the exceptional point, also controlled by microwaves, to enhance measurement sensitivity [63].

A. Quantum enhanced metrology based on flipping trajectory of cold Rydberg gases

Rydberg atomic systems have exhibited rich hysteretic trajectories that arise from interaction-induced non-Hermitian properties [48]. Building on the previous discovery of interaction-induced exceptional points and hysteresis trajectories in cold Rydberg gases [59], Ya-Jun Wang et al. further investigates quantum sensing based on exceptional points [60]. The interplay between the unique non-Hermitian dynamics of Rydberg atom systems and their complex critical properties offers promising opportunities for microwave field sensing applications [60]. When a microwave field is applied to the interacting Rydberg atoms, it induces a change in the energy spectrum, leading to the closure of energy gaps between different eigenstates. This ‘gap-closing’ effect results in the emergence of ‘folded’ hysteresis

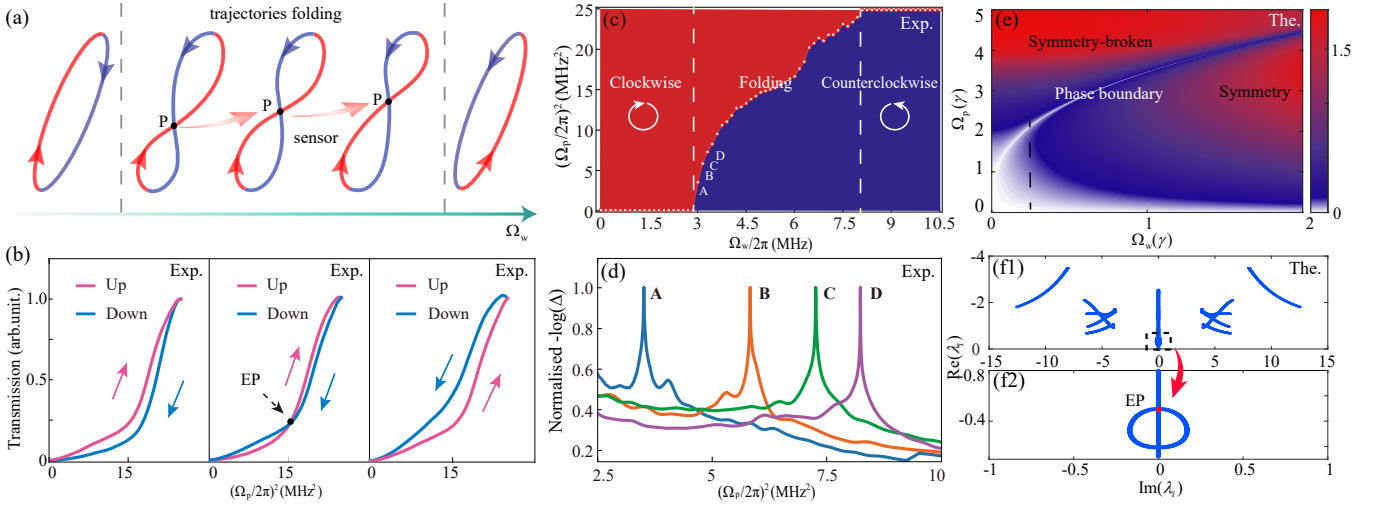


Figure 6. Measured phase diagram of hysteresis trajectories and energy gap phase diagram (Figure adapted from Ref. [60]). (a) Physical schematic diagram. (b) Hysteresis trajectories with microwave field reversal. (c) The measured phase diagram of hysteresis trajectories. The red and blue regions indicate $T_{\text{up}} > T_{\text{down}}$ and $T_{\text{up}} \leq T_{\text{down}}$, respectively. (d) The measured trajectories difference $-\log(\Delta T)$, where blue, orange, green and purple correspond to the data at point A, B, C, and D in (c), respectively. (e) The energy gap is obtained by numerically solving the modulus of $E_2 - E_3$, where the legend represents the magnitude of the energy gap. The white curve with a zero energy gap separates the particle-hole symmetric phase from the symmetry-broken phase. (f₁)-(f₂) The Liouvillian eigenspectrum complex planes of the system in (f₁) and the enlarged view in (f₂), where an Liouvillian exceptional point emerges in the complex planes.

trajectories and the transition between distinct phases. In this scenario, the non-Hermitian properties undergo a dramatic change in response to the microwave field, thereby serving as a valuable resource for demonstrating enhanced sensing. Under the external microwave field driving, the hysteresis trajectories exhibit distinct folding patterns as the Rabi frequency of the probe field is increased and decreased, leading to the formation of microwave field dependent intersection points [Fig. 6(a)]. By analyzing the shifts in the intersection position in response to the external microwave field, the authors achieved high precision measurement of the external field strength, with a sensitivity surpassing the standard quantum limit.

Experimentally, the system's dynamic evolution is monitored by measuring probe transmission. The probe intensity is modulated using a triangular waveform generated by an acousto-optic modulator with a scanning period of T_s , and the transmission trajectories during both the Up and Down processes are recorded [Fig. 6(b)]. Due to the interactions between Rydberg atoms, the interaction-induced dissipation plays a vital role in the system's dynamic evolution. The increase and decrease of Rydberg atoms [by scanning $(\Omega_p/2\pi)^2$] result in asymmetrical responses to probe transmission, generating a hysteresis loop [59]. The measured hysteresis trajectories map the full dynamics onto the parameter space of $(\Omega_p/2\pi)^2$ and $\Omega_w/2\pi$, yielding a phase diagram where regions of $T_{\text{up}} > T_{\text{down}}$ (red) and $T_{\text{up}} \leq T_{\text{down}}$ (blue) are separated by boundaries defined by the white intersection points in Fig. 6(c). The differences in hysteresis trajectories $\Delta T = |T_{\text{up}} - T_{\text{down}}|$ at several positions (A, B, C, D) are shown in Fig. 6(d). As the transmission difference spectra have high discrimination, the intersection points of the trajectories under different microwave fields can be completely separated. In the region of hysteresis trajectory folding, the nonlinear response of the intersection points Ω_w offers a approach to microwave field measurement.

Theoretically, a concise description of open quantum systems is provided by the Lindblad quantum master equation [60]:

$$\dot{\rho} = -i[H, \rho] + \sum_j \left(L_j \rho L_j^\dagger - \frac{1}{2} \{ L_j^\dagger L_j, \rho \} \right) := \mathcal{L} \rho, \quad (23)$$

$$\begin{aligned} H = & - \sum_j [2\Delta_1 \sigma_{ee}^j + (2\Delta_{r_1} + iV_{\text{eff}}) \sigma_{r_1 r_1}^j + 2\Delta_{r_2} \sigma_{r_2 r_2}^j] \\ & + \sum_j [(\Omega_p \sigma_{ge}^j + \Omega_c \sigma_{er_1}^j + \Omega_w \sigma_{r_1 r_2}^j) + H.c.], \end{aligned} \quad (24)$$

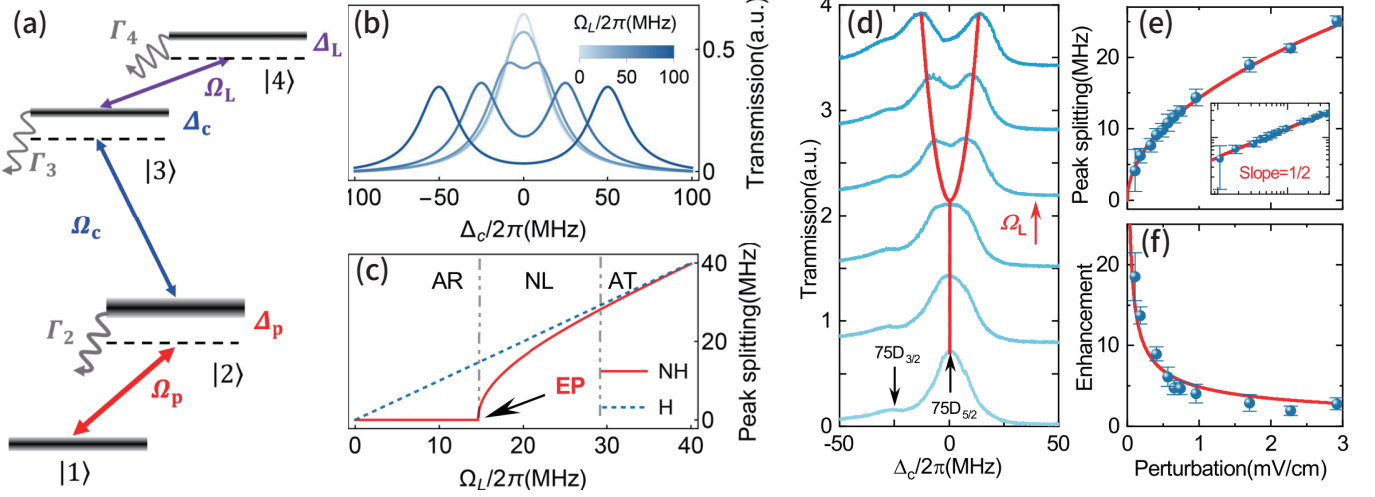


Figure 7. Observing exceptional points in Rydberg atomic ensembles (Figure adapted from Ref. [63]). (a) Energy-level diagram of a four level Rydberg atomic system (b) Transmission spectra of the probe laser as a function of the coupling detuning Δ_c for different values of the microwave Rabi frequency Ω_L . (c) Peak splitting as a function of the microwave Rabi frequency Ω_L . The blue dashed line corresponds to the Hermitian case and the red solid line represents the non-Hermitian case. The regions labeled AR, NL, and AT represent the absorption regime, nonlinear regime, and Autler-Townes regime, respectively. (d) Typical probe transmission spectra as a function of coupling detuning Δ_c for increasing microwave Rabi frequency Ω_L (from bottom to top). The red line traces the central peak positions, revealing nonlinear peak splitting behavior near the exceptional point. (e) Measured peak splitting versus perturbation strength Ω_s . (f) Measured enhancement factor as a function of perturbation strength.

where the operator L_j describes the decay of the system, and \mathcal{L} is a Liouvillian superoperator. The Liouvillian superoperator can be regarded as an effective non-Hermitian operator corresponding to the density matrix, generating the non-unitary evolution of the density matrix. The non-Hermitian Hamiltonian of the system exhibits particle-hole symmetry. However, the closure of the E_2 and E_3 energy gaps leads to the breaking of particle-hole symmetry in the system, resulting in symmetric and symmetry-broken phases. Figure 6(e) is the phase diagram of the energy gap between E_2 and E_3 in the parameter plane of Ω_w and Ω_p . The particle-hole symmetric region and the symmetry-broken region are separated by the gap-closing points (or exceptional points), in which the energy gap approaches zero along the white line. At the phase boundary line, the exceptional points exhibit a non-linear dependence on external parameters (e.g., electric field Ω_w and probe field Ω_p). Furthermore, the Liouvillian eigenspectrum is obtained by solving $\mathcal{L}\hat{\rho}_i = \lambda_i\hat{\rho}_i$, where λ_i and $\hat{\rho}_i$ denote the Liouvillian eigenvalues and eigenstates, respectively. The complex plane distribution of the Liouvillian eigenspectrum is shown in Fig. 6(f₁). As expected, the enlarged view in Fig. 6(f₂) demonstrates the emergence of an exceptional point resulting from the coalescence of eigenvalues and eigenstates.

B. Exceptional Point-enhanced Rydberg Atomic Electrometers

Exceptional points in non-Hermitian systems enable approaches to ultrasensitive metrology. Chao Liang et al. introduced a theoretical framework for Rydberg electrometry based on the Autler-Townes effect under non-Hermitian conditions [63]. They experimentally demonstrated a Rydberg atomic voltmeter that exploits exceptional points for sensitivity enhancement, based on a hot vapor cell. A second-order exceptional point was realized in an effective passive non-Hermitian Hamiltonian, achieved by harnessing the intrinsic dissipation of Rydberg excited states and optimizing the coupling optical fields. In this non-Hermitian system, the Autler-Townes splitting inherently exhibits nonlinear characteristics. Near the exceptional point region, the sensor's responsivity to weak microwave fields can be enhanced by nearly a factor of 20. By coupling the signal microwave field with a controllable local dressing field, amplitude- and phase-sensitive detection was realized. In the nonlinear Autler-Townes region, they observed amplified responses of the Autler-Townes splitting, achieving a sensitivity of $22.68 \text{ nV cm}^{-1}\text{Hz}^{-1/2}$. This result proposes a paradigm for enhanced quantum electrometry by exceptional points, combining the intrinsic field sensitivity of Rydberg atoms with non-Hermitian criticality.

The model is based on the general four-level scheme for Rydberg electrometry. Rydberg atoms are excited using a two-photon excitation scheme, as shown in Fig. 7(a). The effective non-Hermitian Hamiltonian of the system

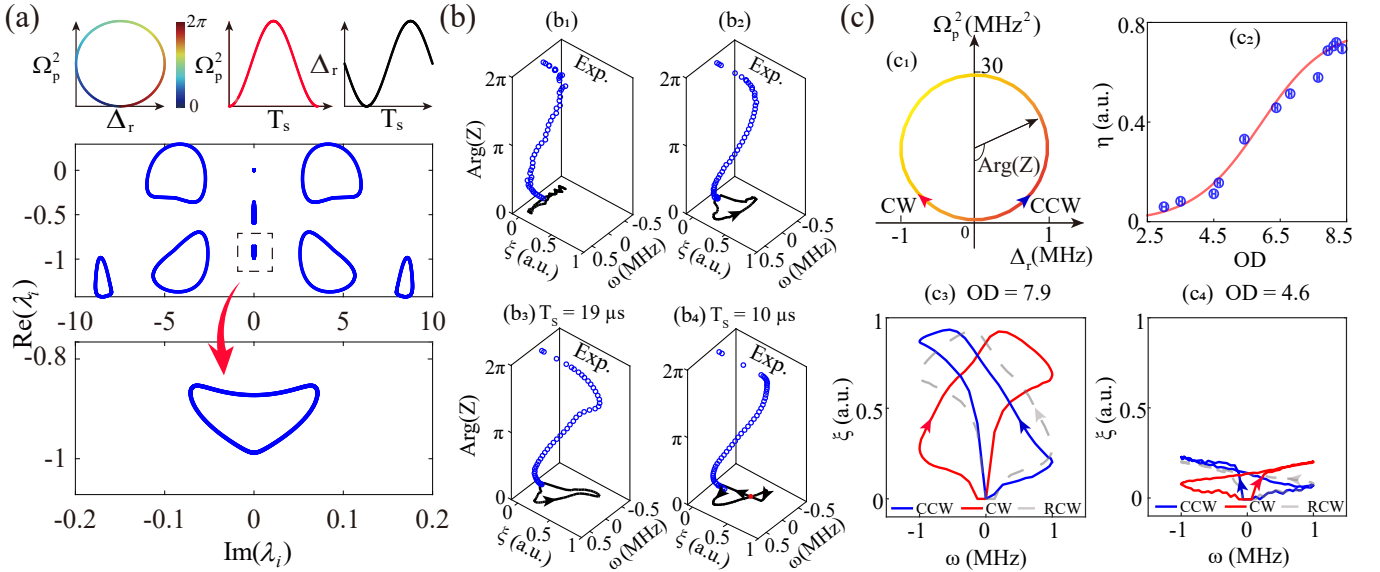


Figure 8. Non-Hermitian spectral topology (Figure adapted from Ref. [54]). (a) Numerical simulations of Liouvillian eigen-spectrum varying with parameter $\text{Arg}(Z)$ on the complex energy plane, where $Z = \Delta_r + i\Omega_p^2$. The enlarged view represents the eigenvalue λ_{rr} of eigenstate ρ_{rr} . The upper panel shows the diagram of changing trends of parameters Ω_p^2 and Δ_r . (b) The evolution trajectory of Rydberg eigenstate in the complex energy plane is strongly correlated with the variation of probe transmission and the energy level detuning Δ_r in the experiment varies with the parameter $\text{Arg}(Z)$, where $Z = \Delta_r + i\Omega_p^2$ in the scanning time of $T_s = 18 \mu\text{s}$. Panels (b₁), (b₂), display the spectral features for $(\Omega_p/2\pi)^2 \in [0, 1] \text{ MHz}^2$, and $(\Omega_p/2\pi)^2 \in [0, 4] \text{ MHz}^2$. The scanning times are as follows: $T_s = 19 \mu\text{s}$ in (b₃), and $T_s = 10 \mu\text{s}$ in (b₄). (c) Chirality symmetry breaking. (c₁) The clockwise (CW) and counterclockwise (CCW) scan paths of the parameters Ω_p^2 and Δ_r , corresponding to the chiral operation. (c₂) The nonreciprocity parameter η as a function of OD, and the red fitting curve. (c₃, c₄) The projections of spectra under two different scanning paths on the parameter plane, at the condition of optical depth OD = 7.9 and OD = 4.6. The grey dash curve denotes the mirror curve of the projected topological trajectory under the clockwise scanning.

reads [63]:

$$\mathcal{H}_{\text{NH}} = \frac{1}{2} \begin{pmatrix} -i\gamma_p & -i\Omega_{\text{eff}} & 0 \\ i\Omega_{\text{eff}} & -i\gamma_c & -\Omega_L \\ 0 & -\Omega_L & 0 \end{pmatrix}. \quad (25)$$

The emergence of the exceptional point divides the system into parity-time symmetry and breaking phases. Far from the exceptional point, the splitting becomes linearly proportional to the perturbation field $\Delta f = \text{Re}(E_+ - E_-) \propto \Omega_s$. Near the exceptional point, the system exhibits a nonlinear response to the electric field, characterized by a square-root scaling of the energy level splitting $\Delta f = \text{Re}(E_+ - E_-) \propto \sqrt{\Omega_s}$. Figure 7(b) is a theoretical simulation of the traditional Autler-Townes splitting in a Hermitian system. The peak-to-peak splitting as a function of Ω_L is plotted in Fig. 7(c) (red curve), with the Hermitian case indicated by the blue dashed line. Three distinct regimes are identified: an absorption regime in the parity-time broken phase; a nonlinear regime near the exceptional point in the parity-time symmetric phase; and a conventional Autler-Townes regime farther away from the exceptional point. Representative experimental results are shown in Fig. 7(d), where the transmission spectra of the probe field are measured as a function of the detuning Δ_c . From bottom to top, the strength of the microwave field Ω_L gradually increases, leading to the progressive splitting of the resonance peak. The red line traces the central peak positions, revealing a nonlinear peak splitting behavior. Figure 7(e) demonstrates a square-root dependence of the peak splitting on the perturbation electric field near the exceptional point. The experimental results exhibit an enhancement of nearly 20-fold in responsivity in the vicinity of the exceptional point, as shown in Fig. 7(f).

VI. TOPOLOGICAL STATES AND NON-HERMITIAN QUANTUM PHASE TRANSITIONS

Topological phases reveal the intrinsic spatial properties preserved by matter during continuous deformations such as stretching and bending, with transitions characterized by changes in topological invariants [33, 131]. The rich properties of Rydberg atoms enable them to serve as a versatile platform for exploring topological states and phase

transitions, while simultaneously introducing greater complexity to the system. Currently, a major challenge is to achieve these phenomena in interacting many-body platforms. Investigating the interaction mechanisms is therefore crucial for understanding how strong interactions and dissipation jointly govern topological phases in open quantum systems.

A. Observation of non-Hermitian topology in cold Rydberg quantum gases

Recently, Jun Zhang et al. experimentally demonstrated non-Hermitian spectral topology in dissipative cold Rydberg atomic gases [54]. To characterize the spectral topology of the system, they presented the Liouvillian space $\mathcal{L}(Z)$ depends on the complex parameter $Z = \Delta_r + i\Omega_p^2$. The results of diagonalizing the system's Liouvillian matrix are shown in Fig. 8(a), where the trajectory of eigenvalues on the complex plane reveals a 'line-gap' topology. As Z varies along a closed contour C_Z in the parameter space, the Liouvillian eigenvalue forms a loop in the complex plane. This loop can wind around a reference energy point λ , giving rise to a nontrivial spectral winding number \mathcal{W}_λ , which is defined as [54, 88, 132]:

$$\mathcal{W}_\lambda = \frac{1}{2\pi i} \oint_{C_Z} d\vec{Z} \cdot \nabla_Z \ln \det (\mathcal{L}(Z) - \lambda I). \quad (26)$$

It counts the number of times the spectrum winds around the reference eigenvalues λ and I is an identity matrix of the same dimension as \mathcal{L} . For a clockwise winding, $\mathcal{W}_\lambda = -1$, while for a counterclockwise winding, $\mathcal{W}_\lambda = 1$.

Experimentally, the topological evolution of the energy spectrum in the complex plane reveals a transition from a Hermitian state (Fig. 8(b₁)) to a non-Hermitian state (Fig. 8(b₂)). Notably, the scanning time governs the dynamic evolution of this topological structure by allowing for the tuning of the effective Rydberg atomic interactions. By tuning the scanning time, the spectral loop can be distorted, leading to a topological phase transition accompanied by a change in the sign of the winding number (see Figs. 8(b₃) and (b₄)). Additionally, by reversing the direction of parameter scanning, differences in spectral loops can be observed (Fig. 8(c)). The distinct separation of the two curves highlights the asymmetry and path-dependence of the system's response, revealing the characteristics of chiral symmetry breaking. The nonreciprocal parameter is defined as $\eta = \oint_{C_Z} d\vec{Z} |O_{RCW}(Z) - O_{CCW}(Z)|$ to quantify the property of the chirality symmetry breaking of the system. Here, $O_{RCW}(Z)$ and $O_{CCW}(Z)$ denote the measured observables along the mirror-symmetric clockwise (RCW) and counterclockwise scanning paths at the complex parameter Z . The parameter η quantifies the relative asymmetry between the system's responses under these two scanning directions. Figure 8 (f) directly presents the variation of the nonreciprocal parameter η with OD.

B. Topological atomic spin wave lattices by dissipative couplings

Topological phases of quantum matter also exhibit fascinating phenomena, such as edge modes unaffected by defects, which hold potential applications in quantum computing [133, 134]. The robustness of edge modes across various lattice systems can largely be attributed to energy gap protection and their connection to topologically nontrivial bands. Symmetry-protected edge modes remain energetically located within the bulk energy gap and are immune to local perturbations. Recently, lattice systems with dissipative coupling exhibit spectral characteristics distinct from coherently coupled networks and may enable topological dissipation. Therefore, dissipative coupling also offers the possibility of designing topological structures.

Dong-Dong Hao et al. experimentally realized a dissipative version of the Su-Schrieffer-Heeger model [30]. Based on a spatial lattice of atomic spin waves in a vapor cell, the experiment utilized an enriched ⁸⁷Rb vapor cell [Fig. 9(a)]. The cell temperature is set to 40°C to maintain a relatively small optical depth. The laser beam was split into several spatially separated beams via polarization-maintaining fibers, forming optical channels within the vapor cell. Each channel established a Λ -type electromagnetically induced transparency configuration involving ground states $|1\rangle$, $|2\rangle$, and an excited state $|3\rangle$. A uniform magnetic field was applied to induce Zeeman shifts in the energy levels, enabling precise tuning of the two-photon detuning δ_B . Spin waves in different optical channels were coupled inhomogeneously through atomic motion. Consequently, a dissipative version of the Su-Schrieffer-Heeger model was implemented by arranging channels with alternating spacings d_1 and d_2 . The non-Hermitian Hamiltonian can be written as [30]:

$$H = i\omega e^{i\delta_B d_1/\nu} \sum_m (|a, m\rangle \langle b, m| + |b, m\rangle \langle a, m|) + i\omega e^{i\delta_B d_2/\nu} \sum_m (|b, m\rangle \langle a, m+1| + |a, m+1\rangle \langle b, m|), \quad (27)$$

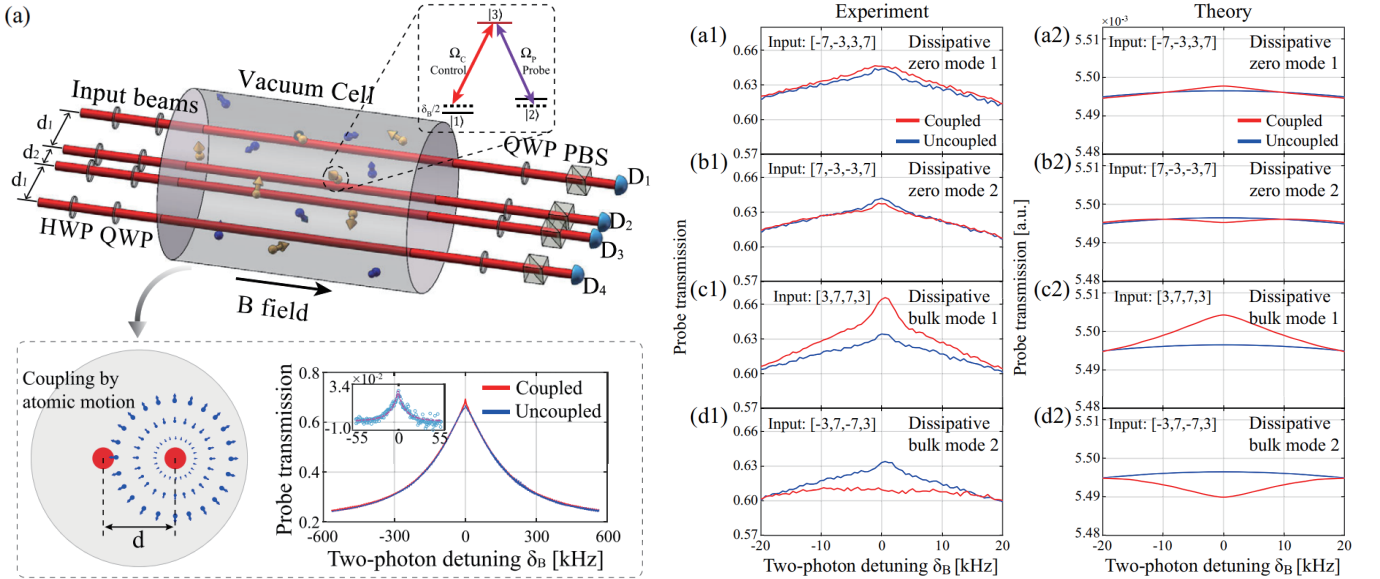


Figure 9. Schematics and principle of atomic vapor cell experiment simulating Su-Schrieffer-Heeger model with dissipative couplings (Figure adapted from Ref. [30]). (a) Setup. Top: several optical channels with designed spacings in the vaporcell create ground state coherences (spin waves) by electromagnetically induced transparency process in each channel. Bottom right: characterization of dissipative coupling rate using a two-channel setting. (a1)–(d1) Measured electromagnetically induced transparency spectra via the probe transmission (normalized to far off resonant 100% transmission), coupled (all channel probes on) and uncoupled (only probe in the detected channel on), for the four input states $[-7, -3, 3, 7]^T$, $[7, -3, -3, 7]^T$, $[3, 7, 7, 3]^T$, $[-3, 7, -7, 3]^T$, respectively. (a2)–(d2) Theoretical calculations of the optical coherences.

where the dissipative coupling rates within and between unit cells, v and w , satisfy $v/w \propto d_2/d_1$. When $\delta_B = 0$, a purely dissipative version of the typical Su-Schrieffer-Heeger model is realized, which possesses chiral symmetry and exhibits a topological dissipative spectrum when $v < w$. This is characterized by edge modes existing within the bulk dissipative gap at zero dissipation rate, whereas the case where $v > w$ is trivial.

In the experiment, transmission spectra for both channels were measured at a relatively high probe power to improve the signal-to-noise ratio, thereby allowing for the extraction of the average eigenvalue. The results show that the electromagnetically induced transparency spectrum for the edge state input nearly coincides with the uncoupled electromagnetically induced transparency spectrum, as shown in Figs. 9(a1)–(b1). In contrast, for the bulk modes in Figs. 9(c1)–(d1), significant changes in both peak intensity and linewidth of the electromagnetically induced transparency spectrum are observed compared to the uncoupled case. Figures 9(a2)–(d2) show the theoretical results obtained by calculating the Hamiltonian, which are consistent with the experimental findings.

C. Probing the topological phase transition using Rydberg atom synthetic dimensions

Synthetic dimensions based on Rydberg atoms offer another highly flexible experimental platform for realizing and probing topological phase transitions. Y. Lu et al. experimentally investigated the topological phase transition in the Su-Schrieffer-Heeger Hamiltonian by constructing a six state synthetic dimension from Rydberg atomic levels [66]. This work demonstrates that even with a finite-sized system, the Su-Schrieffer-Heeger model implemented via Rydberg atom synthetic dimensions enables reliable observation of topological phase transitions through combined spectral and dynamical measurements. The platform is highly extensible: larger systems can be realized by incorporating more Rydberg levels, and more complex lattice geometries or artificial gauge fields can be engineered. This approach opens the experimental avenue for studying topological states and their dynamics in Rydberg atom synthetic dimensions.

In this experiment, a cold gas of ^{84}Sr atoms was used, with six neighboring n^3S_1 Rydberg states ($n \approx 60$) serving as sites in a synthetic lattice. Adjacent states were coupled via two photon microwave transitions, implementing a Su-Schrieffer-Heeger model with alternating strong (J_2) and weak (J_1) tunneling amplitudes, as illustrated in Figs. 10(a)-(b). By tuning the microwave field amplitudes, the tunneling ratio J_1/J_2 could be precisely controlled, enabling systematic exploration of the topological phase transition across the range $J_1/J_2 = \{0.2, 0.5, 1, 2, 5\}$.

By measuring the Rydberg excitation spectrum in the presence of microwave fields, the evolution of the eigenenergy spectrum with the tunneling ratio was directly observed (Figs. 10(c)-(d)). At small values of J_1/J_2 , the spectrum

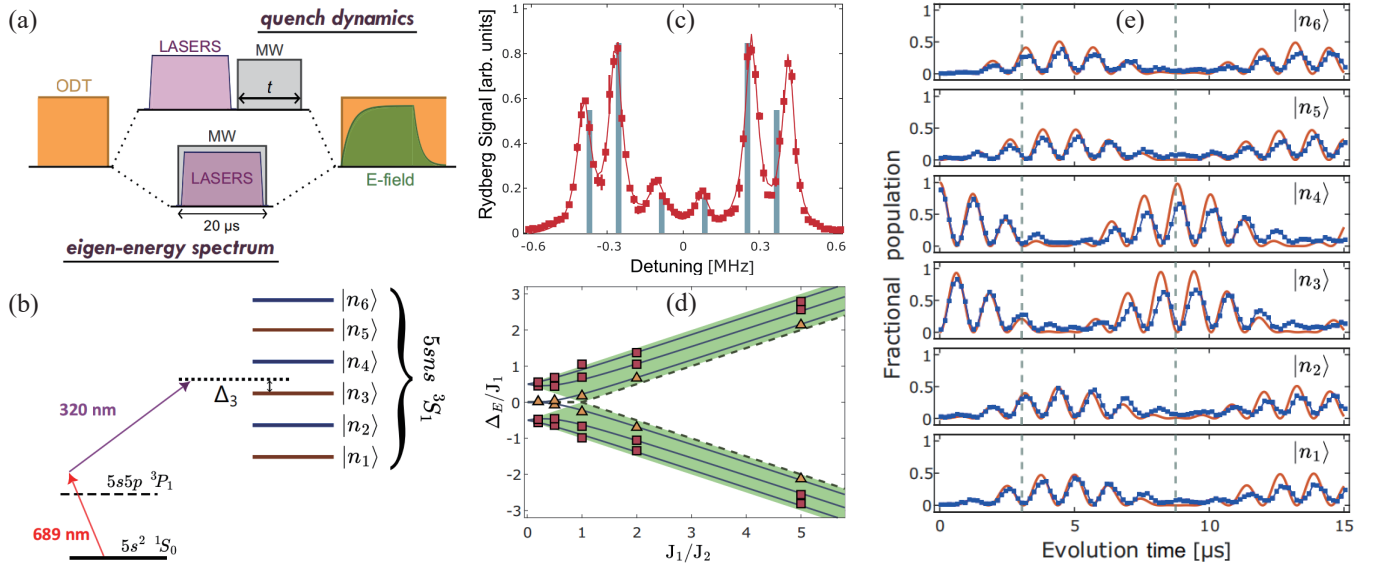


Figure 10. Probing the topological phase transition using Rydberg atom synthetic dimensions (Figure adapted from Ref. [66]). (a) The pulse sequence of an experimental cycle. (b) Experimental realization of the six-site Su-Schrieffer-Heeger model. (c) Rydberg excitation spectrum with the laser frequency scanned across the bare state $|n_2\rangle$ for tunneling ratio $J_1/J_2 = 1$. (d) The eigenenergies measured from the peak positions Δ_E in the Lorentzian fits of the Rydberg excitation spectra at different tunneling ratios $J_1/J_2 = 1$. The triangles and squares denote the edge (at small J_1/J_2) and bulk states, respectively, and the solid lines show the calculated results. (e) Evolution of the fractional populations in each n^3S_1 bare Rydberg state with initial excitation to the fourth state $|n_4\rangle$.

exhibits nearly degenerate zero-energy edge states. As J_1/J_2 increases and crosses the critical value, these edge states disappear, and a bulk band gap opens, further confirming the loss of topological protection. Despite the system consisting of only six states, it captures the essential features of the Su-Schrieffer-Heeger model, including the bulk band structure, edge states, and their behavior near the phase transition. To probe the topological properties of the system, the team combined quench dynamics experiments with spectral measurements. In the quench experiments, the atom was initially excited to a selected Rydberg state, after which the microwave couplings were switched on, and the time evolution of the population in each state was recorded (Fig. 10(e)).

D. Observation of non-Hermitian many-body phase transition in a Rydberg-atom array

Rydberg atom arrays, leveraging their advantages of single-site addressability, highly tunable interactions, and flexible scalability in system size, have emerged as a suitable platform for controllable many-body quantum simulation. Yao-Wen Zhang et al. experimentally implemented a non-Hermitian XY spin chain model in a one-dimensional programmable optical tweezer array [64], a system that exhibits the complex interplay of dissipation and coherent interactions. They observed the parity-time symmetry breaking phase transition, thereby revealing how interactions fundamentally shape non-Hermitian dynamics in a controllable atomic array. It establishes an experimental foundation for exploring non-Hermitian many-body physics beyond the single-particle paradigm in highly controllable quantum simulators.

The core of the experiment lies in engineering an effective non-Hermitian Hamiltonian with parity-time symmetry through microwave field coupling and state-selective dissipation [64]:

$$H_{\text{pt}} = \sum_{i=1}^N \left(\frac{\Omega}{2} \sigma_i^x + i \frac{\Gamma}{4} \sigma_i^z \right) + \sum_{i < j} \frac{V_{ij}}{2} (\sigma_i^x \sigma_j^x + \sigma_i^y \sigma_j^y), \quad (28)$$

where $\sigma_i^{x,y,z}$ are Pauli operators of the i -th atom, Γ is the dissipation rate, and $V_{ij} \propto r_{ij}^{-3}$ is the dipole-dipole exchange interaction. The numerical calculation of eigenvalues is shown in Figs. 11A and B. By precisely tuning the interatomic distance and the microwave Rabi frequency Ω , the system can undergo a phase transition between the parity-time symmetric and symmetry breaking phases. To probe this transition, the research team introduced the Loschmidt Echo as a dynamical observable, defined as the survival probability of the initial state $|0_N\rangle = |\uparrow\uparrow\cdots\uparrow\rangle$ after

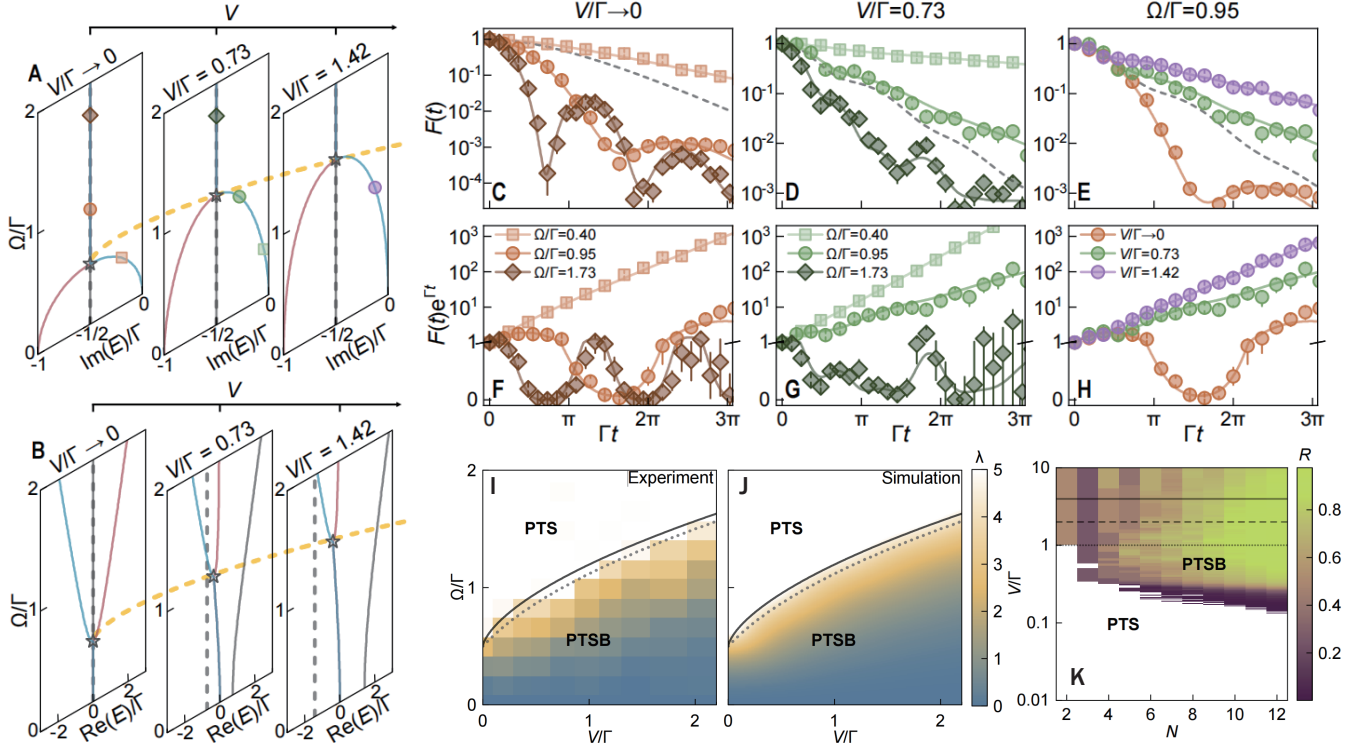


Figure 11. Non-Hermitian spectra, dynamics of Loschmidt Echo, and parity-time phase diagram of interacting Rydberg atoms. (Figure adapted from Ref. [64]). (A-B) Imaginary (A) and real (B) parts of the eigenvalues E . (C-E) Evolution of the Loschmidt Echo (LE) $F(t)$. Solid curves are numerical simulations using the experimental parameters, while dashed curves are simulated results at the exceptional points. (F-H) Scaled Loschmidt Echo, $F(t)e^{\Gamma t}$, corresponding to the data in (C-E). (I-J) Parity-time phase diagram of interacting Rydberg atoms. Measured (I) and simulated (J) phase diagram of parity-time symmetry (PTS) and parity-time symmetry breaking (PTSB). (K) Parity-time phase transition of N Rydberg atoms.

non-Hermitian evolution: $F(t) = |\langle 0_N | \psi_N(t) \rangle|^2$. Experimentally, the measured Loschmidt Echo displays damped oscillations in the parity-time symmetry phase, whereas it follows monotonic exponential decay in the symmetry breaking phase, reflecting the transition from oscillatory to dissipative dynamics (Figs. 11C-E). The scaled Loschmidt Echo $F(t)e^{\Gamma t}$ more clearly reveals persistent oscillations in the parity-time symmetry phase and exponential gain in the symmetry breaking phase (Figs. 11F-H).

Notably, the experiment also observed an interaction-driven shift of the exceptional point (Figs. 11I-J): as the interaction strength V increases, the critical Rabi frequency Ω_c corresponding to the exceptional point rises significantly, demonstrating the ability of many-body interactions to tune the non-Hermitian phase boundary. Further investigation of the dynamical behavior in multi-atom chains ($N \geq 3$) can reveal richer many-body effects, such as size-dependent non-Hermitian blockade. Researchers also prepared a linear array of N Rydberg atoms to experimentally study the size-dependent effects in the parity-time symmetry and breaking phases, as shown in Fig. 11K.

VII. SUMMARY

This review mainly summarizes recent progress in both non-Hermitian physics and Rydberg atomic systems. Non-Hermitian systems, originating from gain, loss, and nonreciprocal coupling, display a range of distinctive phenomena: complex energy spectra, a biorthogonal basis, symmetric and symmetry-broken phases, and nontrivial topological phases. Representative phenomena include spontaneous symmetry breaking, the emergence of exceptional points, sensing enhanced by exceptional points, and non-Hermitian topological structures. These developments have been widely demonstrated in optical, acoustic, electrical, and cold atom platforms.

Rydberg atoms, with their strong interactions and high controllability, have become an important platform for exploring non-Hermitian quantum many-body physics. Many-body interactions can induce effective dissipation, giving rise to tunable non-Hermitian Hamiltonians. The experimental observation of interaction-induced exceptional points, charge-conjugate parity symmetry breaking, and dynamical features such as non-Hermitian hysteresis trajectories

have been reported. Additionally, the role of Liouvillian exceptional points in open quantum dynamics and their connection to chiral state transfer has been demonstrated. Moreover, microwave-induced trajectory intersections provide a mechanism for highly sensitive microwave detection. The implementation of Rydberg electrometers leveraging exceptional points has demonstrated a substantial enhancement in electric field sensing sensitivity.

Recent experiments on dissipative cold Rydberg gases have demonstrated non-Hermitian spectral topology, characterized by non-trivial winding of the eigenvalue spectrum in the complex energy plane. Furthermore, by exploiting motion-induced dissipative couplings, researchers have realized a dissipative topological structure (Su-Schrieffer-Heeger model), enabling the observation of topological edge states. Meanwhile, Rydberg atom synthetic dimensions provide an alternative pathway to realize and probe the Su-Schrieffer-Heeger model, where phase transitions and topological invariants can be reliably extracted even in finite-size systems through combined spectral and dynamical measurements. The programmable atom array platform has demonstrated the observation of non-Hermitian many-body phase transitions and interaction-driven exceptional point shifts, revealing phenomena such as Loschmidt echo dynamics and size-dependent non-Hermitian many-body blockade. These studies collectively establish Rydberg atoms as a powerful platform for investigating topological phenomena, non-Hermitian phase transitions, and critical dynamics in open quantum systems.

ACKNOWLEDGEMENTS

We acknowledge funding from the National Key R and D Program of China (Grant No. 2022YFA1404002), the National Natural Science Foundation of China (Grant Nos. T2495253, 62435018, 125B2085)

AUTHOR CONTRIBUTIONS STATEMENT

This review was written by Ya-Jun Wang and Jun Zhang under the guidance of Dong-Sheng Ding. All authors contributed to discussions regarding the results and the analysis contained in the manuscript.

[1] K. Yokomizo and S. Murakami, Non-bloch band theory of non-hermitian systems, *Phys. Rev. lett.* **123**, 066404 (2019).

[2] K. Kawabata, K. Shiozaki, M. Ueda, and M. Sato, Symmetry and topology in non-hermitian physics, *Phys. Rev. X* **9**, 041015 (2019).

[3] Y. Ashida, Z. Gong, and M. Ueda, Non-hermitian physics, *Advances in Physics* **69**, 249 (2020).

[4] E. J. Bergholtz, J. C. Budich, and F. K. Kunst, Exceptional topology of non-hermitian systems, *Rev. Mod. Phys.* **93**, 015005 (2021).

[5] H. Shen and L. Fu, Quantum oscillation from in-gap states and a non-hermitian landau level problem, *Phys. Rev. lett.* **121**, 026403 (2018).

[6] Y. Nagai, Y. Qi, H. Isobe, V. Kozii, and L. Fu, Dmft reveals the non-hermitian topology and fermi arcs in heavy-fermion systems, *Phys. Rev. lett.* **125**, 227204 (2020).

[7] Y.-C. Wang, J.-S. You, and H.-H. Jen, A non-hermitian optical atomic mirror, *Nat. Commun.* **13**, 4598 (2022).

[8] Z. Li, C. Li, G. Xu, W. Chen, Z. Xiong, H. Jing, J. S. Ho, and C.-W. Qiu, Synergetic positivity of loss and noise in nonlinear non-hermitian resonators, *Sci. Adv.* **9**, eadi0562 (2023).

[9] Q. Chen, S. A. Chen, and Z. Zhu, Weak ergodicity breaking in non-hermitian many-body systems, *SciPost Phys.* **15**, 052 (2023).

[10] P.-R. Han, F. Wu, X.-J. Huang, H.-Z. Wu, C.-L. Zou, W. Yi, M. Zhang, H. Li, K. Xu, D. Zheng, *et al.*, Exceptional entanglement phenomena: Non-hermiticity meeting nonclassicality, *Phys. Rev. lett.* **131**, 260201 (2023).

[11] L. Xiao, K. Wang, D. Qu, H. Gao, Q. Lin, Z. Bian, X. Zhan, and P. Xue, Non-hermitian physics in photonic systems, *Photonics Insights* **4**, R09 (2025).

[12] M. Beasley, D. Lew, and R. Laughlin, Time-reversal symmetry breaking in superconductors: a proposed experimental test, *Phys. Rev. B* **49**, 12330 (1994).

[13] J. Koch, A. A. Houck, K. L. Hur, and S. Girvin, Time-reversal-symmetry breaking in circuit-qed-based photon lattices, *Phys. Rev. A* **82**, 043811 (2010).

[14] K. Kawabata, S. Higashikawa, Z. Gong, Y. Ashida, and M. Ueda, Topological unification of time-reversal and particle-hole symmetries in non-hermitian physics, *Nat. Commun.* **10**, 297 (2019).

[15] S. K. Ghosh, M. Smidman, T. Shang, J. F. Annett, A. D. Hillier, J. Quintanilla, and H. Yuan, Recent progress on superconductors with time-reversal symmetry breaking, *J. Phys. Condens. Matter* **33**, 033001 (2020).

[16] I. Mandal and E. J. Bergholtz, Symmetry and higher-order exceptional points, *Phys. Rev. Lett.* **127**, 186601 (2021).

[17] J. A. Lourenço, G. Higgins, C. Zhang, M. Hennrich, and T. Macrì, Non-hermitian dynamics and pt-symmetry breaking in interacting mesoscopic Rydberg platforms, *Phys. Rev. A* **106**, 023309 (2022).

[18] R. El-Ganainy, K. G. Makris, M. Khajavikhan, Z. H. Musslimani, S. Rotter, and D. N. Christodoulides, Non-hermitian physics and pt symmetry, *Nat. Phys.* **14**, 11 (2018).

[19] J. Li, A. K. Harter, J. Liu, L. de Melo, Y. N. Joglekar, and L. Luo, Observation of parity-time symmetry breaking transitions in a dissipative floquet system of ultracold atoms, *Nat. Commun.* **10**, 855 (2019).

[20] P. Bonderson and C. Nayak, Quasi-topological phases of matter and topological protection, *Phys. Rev. B* **87**, 195451 (2013).

[21] Y. Ren, Z. Qiao, and Q. Niu, Topological phases in two-dimensional materials: a review, *Rep. Prog. Phys.* **79**, 066501 (2016).

[22] G. Ma, M. Xiao, and C. T. Chan, Topological phases in acoustic and mechanical systems, *Nat. Rev. Phys.* **1**, 281 (2019).

[23] S. Barik, A. Karasahin, C. Flower, T. Cai, H. Miyake, W. DeGottardi, M. Hafezi, and E. Waks, A topological quantum optics interface, *Science* **359**, 666 (2018).

[24] M. Parto, Y. G. Liu, B. Bahari, M. Khajavikhan, and D. N. Christodoulides, Non-hermitian and topological photonics: optics at an exceptional point, *Nanophotonics* **10**, 403 (2020).

[25] S. Imhof, C. Berger, F. Bayer, J. Brehm, L. W. Molenkamp, T. Kiessling, F. Schindler, C. H. Lee, M. Greiter, T. Neupert, *et al.*, Topoelectrical-circuit realization of topological corner modes, *Nat. Phys.* **14**, 925 (2018).

[26] P. Roushan, C. Neill, Y. Chen, M. Kolodrubetz, C. Quintana, N. Leung, M. Fang, R. Barends, B. Campbell, Z. Chen, *et al.*, Observation of topological transitions in interacting quantum circuits, *Nature* **515**, 241 (2014).

[27] L. Li, C. H. Lee, and J. Gong, Topological switch for non-hermitian skin effect in cold-atom systems with loss, *Phys. Rev. Lett.* **124**, 250402 (2020).

[28] T. Yoshida, I. Danshita, R. Peters, and N. Kawakami, Reduction of topological z classification in cold-atom systems, *Phys. Rev. Lett.* **121**, 025301 (2018).

[29] S. Lieu, Topological symmetry classes for non-hermitian models and connections to the bosonic bogoliubov-de gennes equation, *Phys. Rev. B* **98**, 115135 (2018).

[30] D. Hao, L. Wang, X. Lu, X. Cao, S. Jia, Y. Hu, and Y. Xiao, Topological atomic spin wave lattices by dissipative couplings, *Phys. Rev. Lett.* **130**, 153602 (2023).

[31] T. M. Philip, M. R. Hirsbrunner, and M. J. Gilbert, Loss of hall conductivity quantization in a non-hermitian quantum anomalous hall insulator, *Phys. Rev. B* **98**, 155430 (2018).

[32] Y. Chen and H. Zhai, Hall conductance of a non-hermitian chern insulator, *Phys. Rev. B* **98**, 245130 (2018).

[33] C. L. Kane and E. J. Mele, Z 2 topological order and the quantum spin hall effect, *Phys. Rev. Lett.* **95**, 146802 (2005).

[34] G. Harari, M. A. Bandres, Y. Lumer, M. C. Rechtsman, Y. D. Chong, M. Khajavikhan, D. N. Christodoulides, and M. Segev, Topological insulator laser: Theory, *Science* **359**, eaar4003 (2018).

[35] M. A. Bandres, S. Wittek, G. Harari, M. Parto, J. Ren, M. Segev, D. N. Christodoulides, and M. Khajavikhan, Topological insulator laser: Experiments, *Science* **359**, eaar4005 (2018).

[36] H. Zhou, C. Peng, Y. Yoon, C. W. Hsu, K. A. Nelson, L. Fu, J. D. Joannopoulos, M. Soljačić, and B. Zhen, Observation of bulk fermi arc and polarization half charge from paired exceptional points, *Science* **359**, 1009 (2018).

[37] V. Kozii and L. Fu, Non-hermitian topological theory of finite-lifetime quasiparticles: Prediction of bulk fermi arc due to exceptional point, *Phys. Rev. B* **109**, 235139 (2024).

[38] J. Hu, R.-Y. Zhang, M. Wang, D. Wang, S. Ma, J. Huang, L. Wang, X. Ouyang, Y. Zhu, H. Jia, *et al.*, Unconventional bulk-fermi-arc links paired third-order exceptional points splitting from a defective triple point, *Commun. Phys.* **8**, 90 (2025).

[39] H. Busche, P. Huillery, S. W. Ball, T. Ilieva, M. P. Jones, and C. S. Adams, Contactless nonlinear optics mediated by long-range Rydberg interactions, *Nat. Phys.* **13**, 655 (2017).

[40] D. Maxwell, D. Szwer, D. Paredes-Barato, H. Busche, J. D. Pritchard, A. Gauguet, K. J. Weatherill, M. Jones, and C. S. Adams, Storage and control of optical photons using Rydberg polaritons, *Phys. Rev. Lett.* **110**, 103001 (2013).

[41] Y. Dudin and A. Kuzmich, Strongly interacting Rydberg excitations of a cold atomic gas, *Science* **336**, 887 (2012).

[42] M. Saffman, T. G. Walker, and K. Mølmer, Quantum information with Rydberg atoms, *Rev. Mod. Phys.* **82**, 2313 (2010).

[43] C. S. Adams, J. D. Pritchard, and J. P. Shaffer, Rydberg atom quantum technologies, *J. Phys. B: At. Mol. Opt. Phys.* **53**, 012002 (2019).

[44] A. Browaeys and T. Lahaye, Many-body physics with individually controlled Rydberg atoms, *Nat. Phys.* **16**, 132 (2020).

[45] D. Ding, Z. Bai, Z. Liu, B. Shi, G. Guo, W. Li, and C. S. Adams, Ergodicity breaking from Rydberg clusters in a driven-dissipative many-body system, *Sci. Adv.* **10**, eadl5893 (2024).

[46] J. B. Balewski, A. T. Krupp, A. Gaj, D. Peter, H. P. Büchler, R. Löw, S. Hofferberth, and T. Pfau, Coupling a single electron to a bose-einstein condensate, *Nature* **502**, 664 (2013).

[47] C.-C. Chien, S. I. Mistakidis, and H. R. Sadeghpour, Breaking and trapping cooper pairs by Rydberg-molecule spectroscopy in atomic fermi superfluids, *Phys. Rev. A* **110**, L051303 (2024).

[48] C. Carr, R. Ritter, C. Wade, C. S. Adams, and K. J. Weatherill, Nonequilibrium phase transition in a dilute Rydberg ensemble, *Phys. Rev. Lett.* **111**, 113901 (2013).

[49] C. Pérez-Espigares, I. Lesanovsky, J. P. Garrahan, and R. Gutiérrez, Glassy dynamics due to a trajectory phase transition in dissipative Rydberg gases, *Phys. Rev. A* **98**, 021804 (2018).

[50] M. Heyl, Dynamical quantum phase transitions: a review, *Rep. Prog. Phys.* **81**, 054001 (2018).

[51] D.-S. Ding, H. Busche, B.-S. Shi, G.-C. Guo, and C. S. Adams, Phase diagram of non-equilibrium phase transition in a strongly-interacting Rydberg atom vapour, *Phys. Rev. X* **10**, 021023 (2020).

[52] D.-S. Ding, Z.-K. Liu, B.-S. Shi, G.-C. Guo, K. Mølmer, and C. S. Adams, Enhanced metrology at the critical point of a many-body Rydberg atomic system, *Nat. Phys.* **18**, 1447 (2022).

[53] S. De Léséleuc, V. Lienhard, P. Scholl, D. Barredo, S. Weber, N. Lang, H. P. Büchler, T. Lahaye, and A. Browaeys, Observation of a symmetry-protected topological phase of interacting bosons with Rydberg atoms, *Science* **365**, 775 (2019).

[54] J. Zhang, Y.-J. Wang, S.-Y. Shao, B. Liu, L.-H. Zhang, Z.-Y. Zhang, X. Liu, C. Yu, Q. Li, H.-C. Chen, *et al.*, Observation of non-hermitian topology in cold Rydberg quantum gases, *arXiv:2509.26256* (2025).

[55] F. M. Gambetta, F. Carollo, M. Marcuzzi, J. P. Garrahan, and I. Lesanovsky, Discrete time crystals in the absence of manifest symmetries or disorder in open quantum systems, *Phys. Rev. Lett.* **122**, 015701 (2019).

[56] X. Wu, Z. Wang, F. Yang, R. Gao, C. Liang, M. K. Tey, X. Li, T. Pohl, and L. You, Dissipative time crystal in a strongly interacting Rydberg gas, *Nat. Phys.* **20** (2024).

[57] B. Liu, L.-H. Zhang, Q.-F. Wang, Y. Ma, T.-Y. Han, J. Zhang, Z.-Y. Zhang, S.-Y. Shao, Q. Li, H.-C. Chen, *et al.*, Higher-order and fractional discrete time crystals in floquet-driven Rydberg atoms, *Nat. Commun.* **15**, 9730 (2024).

[58] B. Liu, L.-H. Zhang, Y. Ma, Q.-F. Wang, T.-Y. Han, J. Zhang, Z.-Y. Zhang, S.-Y. Shao, Q. Li, H.-C. Chen, *et al.*, Bifurcation of time crystals in driven and dissipative Rydberg atomic gas, *Nat. Commun.* **16**, 1419 (2025).

[59] J. Zhang, E.-Z. Li, Y.-J. Wang, B. Liu, L.-H. Zhang, Z.-Y. Zhang, S.-Y. Shao, Q. Li, H.-C. Chen, Y. Ma, *et al.*, Exceptional point and hysteresis trajectories in cold Rydberg atomic gases, *Nat. Commun.* **16**, 3511 (2025).

[60] Y.-J. Wang, J. Zhang, Z.-Y. Zhang, S.-Y. Shao, Q. Li, H.-C. Chen, Y. Ma, T.-Y. Han, Q.-F. Wang, J.-D. Nan, *et al.*, Quantum enhanced metrology based on flipping trajectory of cold Rydberg gases, *Nat. Commun.* **17**, 1160 (2026).

[61] C. Xie, K. Sun, K.-D. Wu, C.-F. Li, G.-C. Guo, W. Yi, and G.-Y. Xiang, Chiral switching of many-body steady states in a dissipative Rydberg gas, *Sci. Bull.* (2025).

[62] T. Sumarac, E. H. Qiu, S. Tsesses, P. Niu, A. J. Menssen, W. Xu, V. Walther, U. Delić, S. Choi, M. D. Lukin, *et al.*, Controlling Rydberg atom-polariton interactions: from exceptional points to fast readout, *arXiv:2601.06345* (2026).

[63] C. Liang, C. Yang, and W. Huang, Exceptional point-enhanced Rydberg atomic electrometers, *arXiv:2506.12861* (2025).

[64] Y.-W. Zhang, B. Xu, Y. Zhou, D.-S. Xiang, H.-X. Liu, P. Zhou, K. Zhang, R. Liao, T. Pohl, W. Li, *et al.*, Observation of non-hermitian many-body phase transition in a Rydberg-atom array, *arXiv:2512.02753* (2025).

[65] S. Kanungo, J. Whalen, Y. Lu, M. Yuan, S. Dasgupta, F. Dunning, K. Hazzard, and T. Killian, Realizing topological edge states with Rydberg-atom synthetic dimensions, *Nat. Commun.* **13**, 972 (2022).

[66] Y. Lu, C. Wang, S. Kanungo, F. Dunning, and T. Killian, Probing the topological phase transition in the su-schrieffer-heeger hamiltonian using Rydberg-atom synthetic dimensions, *Phys. Rev. A* **110**, 023318 (2024).

[67] Y. Lu, C. Wang, S. Kanungo, S. Yoshida, F. Dunning, and T. Killian, Wave-packet dynamics and long-range tunneling within the su-schrieffer-heeger model using Rydberg-atom synthetic dimensions, *Phys. Rev. A* **109**, 032801 (2024).

[68] D. C. Brody, Biorthogonal quantum mechanics, *J. Phys. A: Math. Theor.* **47**, 035305 (2013).

[69] H. Jiang, R. Lü, and S. Chen, Topological invariants, zero mode edge states and finite size effect for a generalized non-reciprocal su-schrieffer-heeger model, *Eur. Phys. J. B* **93**, 125 (2020).

[70] Q.-B. Zeng, B. Zhu, S. Chen, L. You, and R. Lü, Non-hermitian kitaev chain with complex on-site potentials, *Phys. Rev. A* **94**, 022119 (2016).

[71] Z. Shen, Y.-L. Zhang, Y. Chen, C.-L. Zou, Y.-F. Xiao, X.-B. Zou, F.-W. Sun, G.-C. Guo, and C.-H. Dong, Experimental realization of optomechanically induced non-reciprocity, *Nat. Photonics* **10**, 657 (2016).

[72] L. Feng, R. El-Ganainy, and L. Ge, Non-hermitian photonics based on parity-time symmetry, *Nat. Photonics* **11**, 752 (2017).

[73] A. Ghatak, M. Brandenbourger, J. Van Wezel, and C. Coulais, Observation of non-hermitian topology and its bulk-edge correspondence in an active mechanical metamaterial, *Proc. Natl. Acad. Sci.* **117**, 29561 (2020).

[74] M. Fruchart, R. Hanai, P. B. Littlewood, and V. Vitelli, Non-reciprocal phase transitions, *Nature* **592**, 363 (2021).

[75] W. Gou, T. Chen, D. Xie, T. Xiao, T.-S. Deng, B. Gadway, W. Yi, and B. Yan, Tunable nonreciprocal quantum transport through a dissipative aharonov-bohm ring in ultracold atoms, *Phys. Rev. Lett.* **124**, 070402 (2020).

[76] B. Li, Y. Zuo, L.-M. Kuang, H. Jing, and C. Lee, Loss-induced quantum nonreciprocity, *npj Quantum Inf.* **10**, 75 (2024).

[77] W. Ji and X.-G. Wen, Categorical symmetry and noninvertible anomaly in symmetry-breaking and topological phase transitions, *Phys. Rev. Res.* **2**, 033417 (2020).

[78] C. Chen, G. Bernet, M. Bintz, G. Emperauger, L. Leclerc, V. S. Liu, P. Scholl, D. Barredo, J. Hauschild, S. Chatterjee, *et al.*, Continuous symmetry breaking in a two-dimensional Rydberg array, *Nature* **616**, 691 (2023).

[79] C.-K. Chiu, H. Yao, and S. Ryu, Classification of topological insulators and superconductors in the presence of reflection symmetry, *Phys. Rev. B* **88**, 075142 (2013).

[80] C.-K. Chiu, J. C. Teo, A. P. Schnyder, and S. Ryu, Classification of topological quantum matter with symmetries, *Rev. Mod. Phys.* **88**, 035005 (2016).

[81] P. Delplace, T. Yoshida, and Y. Hatsugai, Symmetry-protected multifold exceptional points and their topological characterization, *Phys. Rev. Lett.* **127**, 186602 (2021).

[82] H. Meng, Y. S. Ang, and C. H. Lee, Exceptional points in non-hermitian systems: Applications and recent developments, *Appl. Phys. Lett.* **124** (2024).

[83] B. Midya, H. Zhao, and L. Feng, Non-hermitian photonics promises exceptional topology of light, *Nat. Commun.* **9**, 2674 (2018).

[84] K. Zhang, Z. Yang, and C. Fang, Correspondence between winding numbers and skin modes in non-hermitian systems, *Phys. Rev. Lett.* **125**, 126402 (2020).

[85] N. Okuma, K. Kawabata, K. Shiozaki, and M. Sato, Topological origin of non-hermitian skin effects, *Phys. Rev. Lett.* **124**, 086801 (2020).

[86] Z. Gong, Y. Ashida, K. Kawabata, K. Takasan, S. Higashikawa, and M. Ueda, Topological phases of non-hermitian systems, *Phys. Rev. X* **8**, 031079 (2018).

[87] S. Sarkar, A. Bayat, S. Bose, and R. Ghosh, Exponentially-enhanced quantum sensing with many-body phase transitions, *Nat. Commun.* **16**, 5159 (2025).

[88] J. C. Budich and E. J. Bergholtz, Non-hermitian topological sensors, *Phys. Rev. Lett.* **125**, 180403 (2020).

[89] F. Koch and J. C. Budich, Quantum non-hermitian topological sensors, *Phys. Rev. Res.* **4**, 013113 (2022).

[90] W. Chen, S. Kaya Özdemir, G. Zhao, J. Wiersig, and L. Yang, Exceptional points enhance sensing in an optical microcavity, *Nature* **548**, 192 (2017).

[91] C. H. Lee and R. Thomale, Anatomy of skin modes and topology in non-hermitian systems, *Phys. Rev. B* **99**, 201103 (2019).

[92] L. Xiao, T. Deng, K. Wang, G. Zhu, Z. Wang, W. Yi, and P. Xue, Non-hermitian bulk-boundary correspondence in quantum dynamics, *Nat. Phys.* **16**, 761 (2020).

[93] Y.-X. Xiao, Z.-Q. Zhang, and C. Chan, Restoration of non-hermitian bulk-boundary correspondence by counterbalancing skin effect, *Commun. Phys.* **7**, 140 (2024).

[94] C. H. Lee, L. Li, and J. Gong, Hybrid higher-order skin-topological modes in non-reciprocal systems, *Phys. Rev. Lett.* **123**, 016805 (2019).

[95] X. Zhang, T. Zhang, M.-H. Lu, and Y.-F. Chen, A review on non-hermitian skin effect, *Adv. Phys. X* **7**, 2109431 (2022).

[96] W.-C. Jiang, J. Li, Q.-X. Li, and J.-J. Zhu, The reciprocating and bipolar non-hermitian skin effect engineered by spin-orbit coupling, *Appl. Phys. Lett.* **123** (2023).

[97] C.-H. Zhao, J.-R. Li, C. Jiang, X.-F. Dai, and W.-J. Gong, Topological phase transition and bipolar skin effect in the su-schrieffer-heeger chain with nonreciprocal spin-orbital coupling, *Phys. Rev. B* **110**, 155432 (2024).

[98] Y. Qin, Y. S. Ang, C. H. Lee, and L. Li, Many-body critical non-hermitian skin effect, *Commun. Phys.* (2025).

[99] Y.-M. Hu, Z. Wang, B. Lian, and Z. Wang, Many-body non-hermitian skin effect with exact steady states in dissipative lattice gauge theory, *Phys. Rev. Lett.* (2025).

[100] H. Yu-Min, S. Fei, and W. Zhong, Generalized brillouin zone and non-hermitian band theory, *Acta Phys. Sin.* **70** (2021).

[101] W. Chen, M. Abbasi, B. Ha, S. Erdamar, Y. N. Joglekar, and K. W. Murch, Decoherence-induced exceptional points in a dissipative superconducting qubit, *Phys. Rev. lett.* **128**, 110402 (2022).

[102] K. Sun and W. Yi, Chiral state transfer under dephasing, *Phys. Rev. A* **108**, 013302 (2023).

[103] H. Gao, K. Sun, D. Qu, K. Wang, L. Xiao, W. Yi, and P. Xue, Photonic chiral state transfer near the liouvillian exceptional point, *Phys. Rev. lett.* **134**, 146602 (2025).

[104] F. Bariani, P. M. Goldbart, and T. Kennedy, Dephasing dynamics of Rydberg atom spin waves, *Phys. Rev. A* **86**, 041802 (2012).

[105] J. Ningyuan, A. Georgakopoulos, A. Ryou, N. Schine, A. Sommer, and J. Simon, Observation and characterization of cavity Rydberg polaritons, *Phys. Rev. A* **93**, 041802 (2016).

[106] F. Ripka, Y.-H. Chen, R. Löw, and T. Pfau, Rydberg polaritons in a thermal vapor, *Phys. Rev. A* **93**, 053429 (2016).

[107] X. Shu, Q. Zhong, K. Hong, O. You, J. Wang, G. Hu, A. Alù, S. Zhang, D. N. Christodoulides, and L. Chen, Chiral transmission by an open evolution trajectory in a non-hermitian system, *Light Sci. Appl.* **13**, 65 (2024).

[108] C. Wang, X. Jiang, G. Zhao, M. Zhang, C. W. Hsu, B. Peng, A. D. Stone, L. Jiang, and L. Yang, Electromagnetically induced transparency at a chiral exceptional point, *Nat. Phys.* **16**, 334 (2020).

[109] Y. Huang, Y. Shen, C. Min, S. Fan, and G. Veronis, Unidirectional reflectionless light propagation at exceptional points, *Nanophotonics* **6**, 977 (2017).

[110] C. X. Du, G. Wang, Y. Zhang, and J. H. Wu, Light transfer transitions beyond higher-order exceptional points in parity-time and anti-parity-time symmetric waveguide arrays, *Opt. Express* **30**, 20088 (2022).

[111] F. Ding, Y. Deng, C. Meng, P. C. Thrane, and S. I. Bozhevolnyi, Electrically tunable topological phase transition in non-hermitian optical mems metasurfaces, *Sci. Adv.* **10**, eadl4661 (2024).

[112] J. Gong and C. H. Lee, Topological phase transitions have never been faster, *Nat. Phys.* **20**, 12 (2024).

[113] A. Li, H. Wei, M. Cotrufo, W. Chen, S. Mann, X. Ni, B. Xu, J. Chen, J. Wang, S. Fan, *et al.*, Exceptional points and non-hermitian photonics at the nanoscale, *Nat. Nanotechnol.* **18**, 706 (2023).

[114] M. I. Rosa, M. Mazzotti, and M. Ruzzene, Exceptional points and enhanced sensitivity in pt-symmetric continuous elastic media, *J. Mech. Phys. Solids.* **149**, 104325 (2021).

[115] M. Yang, L. Zhu, Q. Zhong, R. El-Ganainy, and P.-Y. Chen, Spectral sensitivity near exceptional points as a resource for hardware encryption, *Nat. Commun.* **14**, 1145 (2023).

[116] W. Chen, M. Abbasi, Y. N. Joglekar, and K. W. Murch, Quantum jumps in the non-hermitian dynamics of a superconducting qubit, *Phys. Rev. lett.* **127**, 140504 (2021).

[117] X.-L. Zhang, S. Wang, B. Hou, and C. Chan, Dynamically encircling exceptional points: in situ control of encircling loops and the role of the starting point, *Phys. Rev. X* **8**, 021066 (2018).

[118] A. Schreiber, A. Gábris, P. P. Rohde, K. Laiho, M. Štefaňák, V. Potoček, C. Hamilton, I. Jex, and C. Silberhorn, A 2d quantum walk simulation of two-particle dynamics, *Science* **336**, 55 (2012).

[119] Z.-K. Liu, L.-H. Zhang, B. Liu, Z.-Y. Zhang, G.-C. Guo, D.-S. Ding, and B.-S. Shi, Deep learning enhanced Rydberg multifrequency microwave recognition, *Nature communications* **13**, 1997 (2022).

[120] J. Zhang, L.-H. Zhang, B. Liu, Z.-Y. Zhang, S.-Y. Shao, Q. Li, H.-C. Chen, Z.-K. Liu, Y. Ma, T.-Y. Han, *et al.*, Early warning signals of the tipping point in strongly interacting Rydberg atoms, *Phys. Rev. Lett.* **133**, 243601 (2024).

- [121] L.-H. Zhang, B. Liu, Z.-K. Liu, Z.-Y. Zhang, S.-Y. Shao, Q.-F. Wang, Y. Ma, T.-Y. Han, G.-C. Guo, D.-S. Ding, *et al.*, Ultra-wide dual-band Rydberg atomic receiver based on space division multiplexing radio-frequency chip modules, *Chip* **3**, 100089 (2024).
- [122] N. Schlossberger, N. Prajapati, S. Berweger, A. P. Rotunno, A. B. Artusio-Glimpse, M. T. Simons, A. A. Sheikh, E. B. Norrgard, S. P. Eckel, and C. L. Holloway, Rydberg states of alkali atoms in atomic vapour as si-traceable field probes and communications receivers, *Nat. Rev. Phys.* **6**, 606 (2024).
- [123] H. Zhang, Y. Ma, K. Liao, W. Yang, Z. Liu, D. Ding, H. Yan, W. Li, and L. Zhang, Rydberg atom electric field sensing for metrology, communication and hybrid quantum systems, *Sci. Bull.* **69**, 1515 (2024).
- [124] J. A. Sedlacek, A. Schwettmann, H. Kübler, R. Löw, T. Pfau, and J. P. Shaffer, Microwave electrometry with Rydberg atoms in a vapour cell using bright atomic resonances, *Nat. Phys.* **8**, 819 (2012).
- [125] J. Sedlacek, A. Schwettmann, H. Kübler, and J. Shaffer, Atom-based vector microwave electrometry using rubidium Rydberg atoms in a vapor cell, *Phys. Rev. lett.* **111**, 063001 (2013).
- [126] H. Hodaei, A. U. Hassan, S. Wittek, H. Garcia-Gracia, R. El-Ganainy, D. N. Christodoulides, and M. Khajavikhan, Enhanced sensitivity at higher-order exceptional points, *Nature* **548**, 187 (2017).
- [127] J.-H. Park, A. Nda, W. Cai, L. Hsu, A. Kodigala, T. Lepetit, Y.-H. Lo, and B. Kanté, Symmetry-breaking-induced plasmonic exceptional points and nanoscale sensing, *Nat. Phys.* **16**, 462 (2020).
- [128] R. Kononchuk, J. Cai, F. Ellis, R. Thevamaran, and T. Kottos, Exceptional-point-based accelerometers with enhanced signal-to-noise ratio, *Nature* **607**, 697 (2022).
- [129] Z. Li, C. Li, Z. Xiong, G. Xu, Y. R. Wang, X. Tian, X. Yang, Z. Liu, Q. Zeng, R. Lin, *et al.*, Stochastic exceptional points for noise-assisted sensing, *Phys. Rev. lett.* **130**, 227201 (2023).
- [130] C. Liang, Y. Tang, A.-N. Xu, and Y.-C. Liu, Observation of exceptional points in thermal atomic ensembles, *Phys. Rev. lett.* **130**, 263601 (2023).
- [131] M. Konig, S. Wiedmann, C. Brune, A. Roth, H. Buhmann, L. W. Molenkamp, X.-L. Qi, and S.-C. Zhang, Quantum spin hall insulator state in hgte quantum wells, *Science* **318**, 766 (2007).
- [132] K. Wang, A. Dutt, K. Y. Yang, C. C. Wojcik, J. Vučović, and S. Fan, Generating arbitrary topological windings of a non-hermitian band, *Science* **371**, 1240 (2021).
- [133] C. Nayak, S. H. Simon, A. Stern, M. Freedman, and S. Das Sarma, Non-abelian anyons and topological quantum computation, *Rev. Mod. Phys.* **80**, 1083 (2008).
- [134] B. Field and T. Simula, Introduction to topological quantum computation with non-abelian anyons, *Quantum Sci. Technol.* **3**, 045004 (2018).